

Correcting heading errors in optically pumped magnetometers through microwave interrogation

C. Kiehl,^{1,2,*} T. S. Menon,^{1,2} S. Knappe,^{3,4} T. Thiele,⁵ and C. A. Regal^{1,2}

¹*JILA, National Institute of Standards and Technology and University of Colorado, Boulder, Colorado 80309, USA*

²*Department of Physics, University of Colorado, Boulder, Colorado 80309, USA*

³*Paul M. Rady Department of Mechanical Engineering,
University of Colorado, Boulder, Colorado 80309, USA*

⁴*FieldLine Inc., Boulder CO 80301, USA*

⁵*Zurich Instruments AG, CH-8005 Zurich, Switzerland*

We demonstrate how to measure in-situ for heading errors of optically pumped magnetometers in geomagnetic fields. For this, we implement microwave-driven Rabi oscillations and Ramsey interferometry on hyperfine transitions as two independent methods to detect scalar systematics of free induction decay (FID) signals. We showcase the wide applicability of this technique by operating in the challenging parameter regime of compact vapor cells with imperfect pumping and high buffer gas pressure. In this system, we achieve suppression of large inaccuracies arising from nonlinear Zeeman (NLZ) shifts by up to a factor of 10 to levels below 0.6 nT. In the Ramsey method we accomplish this, even in arbitrary magnetic field directions, by employing a hyper-Ramsey protocol and optical pumping with adiabatic power ramps. For the Rabi technique, this level of accuracy is reached, despite associated drive-dependent shifts, by referencing Rabi frequency measurements to a complete atom-microwave coupling model that incorporates the microwave polarization structure.

Optically pumped magnetometers (OPMs) are state-of-the-art sensors that can reach sensitivities below 1 fT/ $\sqrt{\text{Hz}}$ [1–4], enable precise detection of biomagnetic signals [5–7], and push the boundaries for scientific exploration by aiding in searches for permanent electron dipole moments [8, 9] and dark matter [10, 11]. Practical use of OPMs in geomagnetic fields such as navigation [12, 13], geophysics [14, 15], space [16–18], and unexploded ordnance detection [19, 20] requires addressing systematic errors that depend on the orientation of the sensor with respect to the magnetic field known as heading errors. For the most common OPMs made of alkali atoms the dominant heading error at geomagnetic fields is on the order of 10 nT. This systematic error manifests from unknown strengths of unresolved frequency components in the magnetometer signal arising from nonlinear Zeeman (NLZ) shifts from each of the ground state hyperfine manifolds [21, 22].

Only in regimes of narrow magnetic resonances [23] and high spin polarization can this heading error be accurately modeled to 0.1 nT [22]. In MEMS vapor cells, these regimes often become unfeasible due to line broadening from atomic collisions and the challenges associated with implementing fast, high-fidelity optical pumping using modest pump powers. Various other approaches have been developed to mitigate heading error including spin locking [24, 25], light polarization modulation [26], double-pass configurations [27], double-modulated synchronous pumping [28], and leverage of tensor light-shifts [29], but all these approaches neglect frequency shifts arising from the different Zeeman resonances between the $F = I \pm 1/2$ manifolds and have their own practical challenges. Furthermore, methods that utilize

higher-order polarization moments [30–32] are not feasible in compact OPM packages with high buffer gas pressures [33]. CPT magnetometry [34, 35] holds promise for high scalar accuracy by detecting multiple hyperfine resonances to address NLZ systematics, though sub-nT accuracy in microfabricated cells remains elusive to date.

Sensitive hyperfine spectroscopy in microfabricated cells has been demonstrated with pulsed [36] and continuous [37, 38] microwave interrogation. Although both of these domains show promise for accurate magnetic sensing, managing systematic shifts in arbitrary field directions remains an issue. Rabi oscillations, for example, that utilize uninterrupted microwave interrogation, enable self-calibrated vector operation [39], but are highly sensitive to systematic shifts from off-resonant driving. Conversely, Ramsey interferometry protocols employed for spectroscopy of hyperfine transitions, as implemented in vapor cell atomic clocks [36, 40, 41], utilize short periods of microwave interrogation to mitigate off-resonant driving, but require linearly polarized microwave sources along a well-defined magnetic field. In this Letter, we solve these microwave interrogation challenges and directly measure the heading error of a microfabricated OPM based on free induction decay (FID) with sub-nT accuracy.

Specifically, we use Rabi and Ramsey frequency spectroscopy that respectively use continuous and pulsed microwave interrogation to detect Zeeman shifts between four hyperfine transitions of ^{87}Rb shown in Fig. 1a. Both techniques can be applied at the same set of vapor cell parameters used for sensitive FID measurements. In Rabi frequency spectroscopy, an atom-microwave Hamiltonian that utilizes calibrated microwave polarization ellipse (MPE) parameters [39] accurately models Rabi oscillation frequencies despite frequency shifts due to off-resonant driving. In contrast, Ramsey frequency spectroscopy does not directly model atom-microwave cou-

* christopher.kiehl@colorado.edu

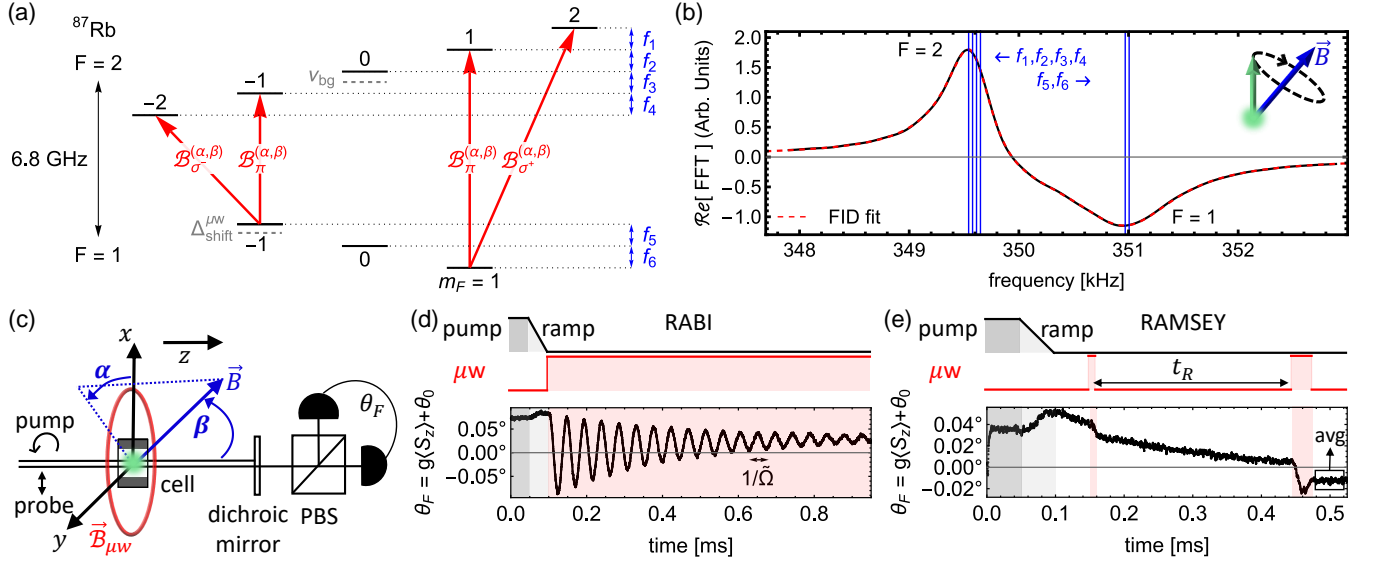


FIG. 1. (a) Energy-level diagram showing the four hyperfine transitions used in Rabi and Ramsey frequency spectroscopy to correct FID heading error. Nonlinear Zeeman splittings f_i (blue) contribute to the Larmor FID signal. Buffer gas pressure shift $\nu_{\text{bg}} \approx 88$ kHz further shifts the hyperfine manifolds. (b) FID signal measured at $\beta = 106^\circ$ in the regime of low-polarization pumping that contains both $F = 1$ and $F = 2$ precession frequencies. Heading errors arise due to the uncertainty in the amplitudes and relative phases of the nonlinear Zeeman frequencies (blue lines). (c) Magnetometer apparatus to measure magnetic fields with direction specified by azimuthal (α) and polar (β) angles. (d,e) Rabi and Ramsey pulse sequences evaluated at $\beta = 35^\circ$ and plotted with a moving average of 10 data points, respectively.

pling, but instead mitigates systematics by varying both the Ramsey time t_R and microwave detuning within a $\pi/2 - t_R - 3\pi/2$ hyper-Ramsey sequence [42]. To prevent signal degradation in arbitrary magnetic field directions, both techniques employ adiabatic power ramps during optical pumping to suppress Larmor precession. We compare these two methods to FID measurements over a range of DC magnetic field directions at $50 \mu\text{T}$. We find the Rabi and Ramsey techniques, despite their distinct concepts, both measure the FID heading error with agreement to within 0.6 nT. From theoretical simulations, we find that the fundamental accuracy of both approaches is within 0.4 nT due to spin-exchange frequency shifts [43, 44].

The magnetometer apparatus [Fig. 1c] consists of a $3 \times 3 \times 2$ mm³ microfabricated vapor cell with a single optical axis, heated to near 100°C , and filled with 180 Torr of N_2 buffer gas. At this buffer gas pressure, Rb-N_2 collisions broaden the optical D1 and D2 transitions to 5.6 GHz. The vapor cell is contained within a rectangular microwave cavity that is the source for driving hyperfine transitions and is detailed in [37]. A 3D coil system defines an orthogonal reference frame (x, y, z), where a calibration corrects for non-orthogonal misalignments between the coil pairs (Supplementary Material [45]). This coil system generates a programmable $50 \mu\text{T}$ magnetic field \vec{B} , defined by azimuthal and polar angles α and β . Along the single optical axis propagates a 795 nm elliptically polarized pump beam, tuned within a few GHz of the D1 line, and a 1 mW probe beam blue-detuned by

170 GHz from the 780 nm D_2 line. A polarimeter detects the Faraday rotation $\theta_F = g\langle S_z \rangle + \theta_0$ of the probe beam expressed in terms of the macroscopic z -component of the electron spin, a coupling coefficient g , and an offset θ_0 [46].

For comparative demonstration, we study FID spin-precession signals with low atomic spin polarization where no accurate physical models for heading errors exist. To initiate FID measurements in this low polarization regime, a $100 \mu\text{s}$ pulse of pump light at 400 mW polarizes atomic spins along the pump beam. In this low spin polarization regime, the FID spectrum [Fig. 1b] consists of both, $F = 1$ and $F = 2$ Zeeman resonances that are separated at $50 \mu\text{T}$ by 1.4 kHz. The NLZ effect splits these resonances into frequency components $\{f_1, \dots, f_6\}$ separated by 36 Hz. We model the FID spectrum as two resonances $f_{L,\pm}(B) \approx \mu_B(g_s - g_i \pm 4g_i)B/4h$ that are the mean Zeeman splitting across the magnetic sublevels for the $F = I \pm 1/2$ manifolds, where $I = 3/2$ is the nuclear spin, g_s and g_i are the electronic and nuclear Landé g -factors, h is Planck's constant, μ_B is the Bohr magneton, and B is the magnetic field strength. The real component of the FID signal's Fourier transform in this model is given by

$$\text{Re}[\text{FFT}] = \sum_{j=\pm} a_j \frac{\cos[\phi_j] - \sin[\phi_j](f - f_{L,j})}{(f - f_{L,j})^2 + w_j^2/4} \quad (1)$$

where $\phi_{\pm} = 2\pi f_{L,\pm}t_0 \pm \phi/2$ are phase shifts due to a starting time offset t_0 with ϕ being a relative phase between the $I \pm 1/2$ resonances respectively. Here the

strength and broadening of this signal is given by amplitudes a_{\pm} and linewidths $w_{\pm} \approx 1$ kHz. Based on the initial atomic state and the direction of \vec{B} , heading error arises in this model from the unresolved NLZ frequency components that bias the observed resonances from $f_{L,\pm}$.

Rabi and Ramsey frequency spectroscopy avoid these heading errors by detecting Zeeman shifts between resolved hyperfine transitions highlighted in Fig. 1a. To make these measurements in arbitrary magnetic field directions, we first optically pump the atomic ensemble for 50 μ s at 100 mW and then linearly ramp off the pump power over the next 50 μ s [Fig. 1(d,e)]. This linear ramp suppresses Larmor precession by adiabatically orienting the atomic spins along the magnetic field \vec{B} [45].

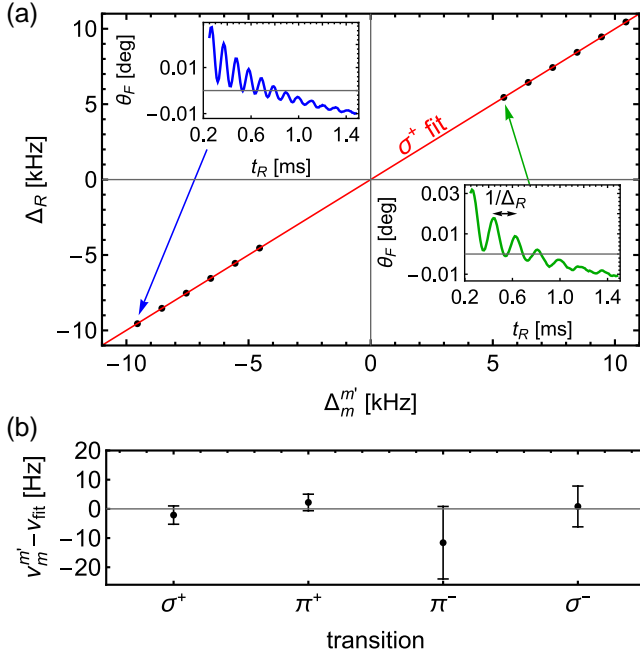


FIG. 2. Ramsey frequency spectroscopy at $\beta = 35^\circ$. (a) Ramsey frequency vs microwave detuning for the σ^+ transition. Insets show measured Ramsey fringes as a function of the Ramsey time t_R . A linear fit (red) extracts the microwave resonance. (b) Residuals of fitting Eq. (2) to the measured hyperfine resonances. Error bars show 68% confidence interval.

Ramsey frequency spectroscopy utilizes pulsed microwave interrogation to accurately measure any hyperfine resonance $\nu_m^{m'} \approx 6.8$ GHz between sublevels $|1, m\rangle$ and $|2, m'\rangle$ without exact knowledge of off-resonant driving. This is achieved through a $\pi/2 - t_R - 3\pi/2$ hyper-Ramsey pulse sequence [42] with $t_{\pi/2} = 4/\tilde{\Omega}_m^{m'} \approx 10$ μ s [Fig. 1e]. Satisfying this particular $t_{\pi/2}$ required manual adjustments to the microwave power at each magnetic field direction and hyperfine transition such that the generalized Rabi frequency satisfied $\tilde{\Omega}_m^{m'} \approx 25$ kHz. Importantly after each pulse sequence, we average the resulting Faraday signal for 50 μ s to filter out residual 350 kHz Larmor precession [Fig. 1e].

By varying the Ramsey free evolution time t_R between 0.2 ms and 1.43 ms at 10 μ s spacing, we measure Ramsey fringes at each microwave detuning as shown in the insets of Fig. 2a. We fit these Ramsey fringes in the time-domain using an exponentially decaying sinusoid [45] and force the fringe frequencies Δ_R to be either positive or negative according to the sign of the microwave detuning $\Delta_m^{m'} = \nu_{\mu w} - \nu_m^{m'}$. Without influence from systematic shifts, $\Delta_R = \Delta_m^{m'}$. We choose 6 microwave detunings $\Delta_m^{m'} \in [5, 10]$ kHz below and above each transition resonance as shown for the σ^+ transition in Fig. 2a. All of these measurements are taken in random order to mitigate systematics from time-dependent drifts in the microwave field. By linear fitting Δ_R as a function of the microwave frequency $\nu_{\mu w}$, the x-intercept measures $\nu_m^{m'}$. The magnetic field B and the pressure shift arising from N_2 buffer gas collisions $\nu_{bg} \approx 88$ kHz are obtained by fitting [Fig. 2b] $\nu_m^{m'}$ measurements to

$$\frac{h\nu_m^{m'}}{\Delta E} = \frac{m' - m}{g_s/g_i - 1}x + \frac{1}{2} \sum_{M=m, m'} \sqrt{1 + \frac{4Mx}{2I+1} + x^2} \quad (2)$$

where $x = (g_s - g_i)\mu_B B / \Delta E$ and $\Delta E = (A + h\nu_{bg}/2)(I + 1/2)$ is the hyperfine splitting expressed in terms of the magnetic dipole hyperfine constant A .

Alternatively, Rabi frequency spectroscopy [Fig. 3a] measures these hyperfine resonances from the detuning $\Delta_m^{m'}$ dependence of generalized Rabi frequencies $(\tilde{\Omega}_m^{m'})^2 \approx (\Delta_m^{m'})^2 + |\Omega_m^{m'}|^2$ that are fitted from Rabi oscillations using an exponentially decaying sinusoid [45]. Unlike Ramsey frequency spectroscopy, this approach demands precise modeling of atom-microwave coupling to accommodate for frequency shifts from off-resonant driving. At a microwave frequency $\nu_{\mu w}$, the atom-microwave coupling is quantified by the following Hamiltonian

$$H = \mathcal{M}[(A + h\frac{\nu_{bg}}{2})\mathbf{S} \cdot \mathbf{I} + \mu_B(g_s S_z + g_i I_z)B]\mathcal{M}^\dagger - I_2 h\nu_{\mu w} + \sum_{|m-m'| \leq 1} \frac{h}{2} [\langle 2, m' | \Omega_m^{m'} | 1, m \rangle + \text{h.c.}] \quad (3)$$

where I_2 is the $F = 2$ identity operator. In order to preserve NLZ effects during the rotating-wave approximation (RWA), we work in a modified hyperfine basis $|\bar{F}, \bar{m}\rangle = \mathcal{M}|F, m\rangle$ with \mathcal{M} being defined as the operator that diagonalizes the hyperfine and Zeeman terms in the first line of Eq. (3). An analytical expression for \mathcal{M} is shown in the Supplementary Material [45]. The Rabi frequency is given by

$$\Omega_m^{m'} = \mu_m^{m'} \mathcal{B}_k^{(\alpha, \beta)} / h \quad (4)$$

where $\mu_m^{m'}$ denotes the corresponding magnetic transition dipole moment [45] and $k = \pm, \pi$ denotes the polarization of the hyperfine transition. The spherical microwave components [Fig. 1a]

$$\mathcal{B}_k^{(\alpha, \beta)} = R_z(\alpha)R_y(\beta)\{\mathcal{B}_x e^{-i\phi_x}, \mathcal{B}_y e^{-i\phi_y}, \mathcal{B}_z\} \cdot \hat{\mathbf{e}}_k \quad (5)$$

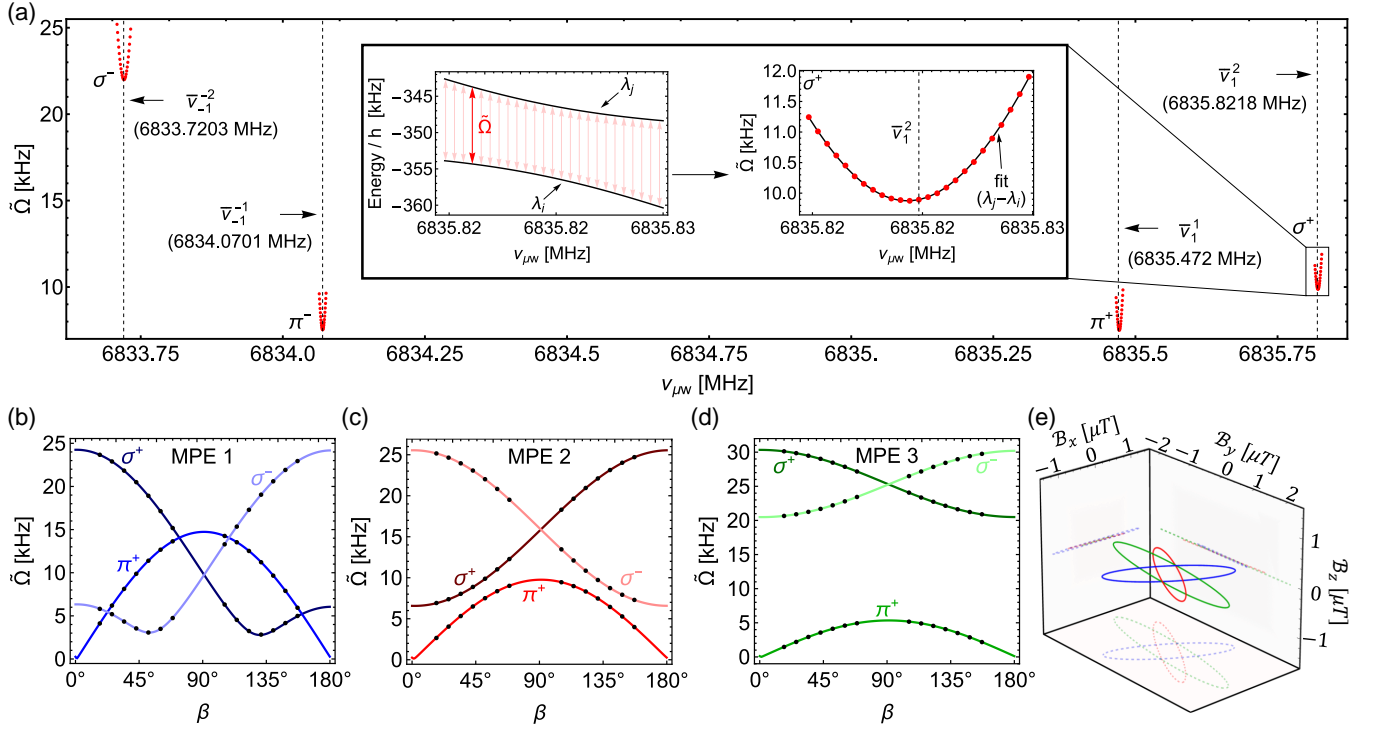


FIG. 3. Rabi frequency spectroscopy and microwave polarization ellipse calibration (a) Generalized Rabi frequency measurements at $\beta = 35^\circ$, driven by MPE 2, with a center microwave frequencies $\bar{\nu}_m^{m'}$ (dashed lines). The inset shows a fit of the σ^+ transition using the eigenstates of H defined in Eq. (3). (b-d) Polar angle dependence of Rabi-frequency measurements for the σ^+ , π^+ , and σ^- hyperfine transitions. Solid lines show fits to calibrate the polarization ellipses. (e) Fitted polarization ellipses.

are defined in terms of an MPE phasor that is projected onto the spherical basis $\epsilon_\pm = \{\frac{1}{\sqrt{2}}, \mp \frac{i}{\sqrt{2}}, 0\}$ and $\epsilon_\pi = \{0, 0, 1\}$. This MPE phasor contains the three microwave amplitudes $(\mathcal{B}_x, \mathcal{B}_y, \mathcal{B}_z)$ and two relative phases (ϕ_x, ϕ_y) that fully define any MPE [39]. To account for different magnetic field directions (α, β) in the lab frame, we assume, without loss of generality, that the magnetic field \vec{B} points along z and rotate the MPE phasor using 3D rotation operators $R_{y,z}$.

The atom-microwave Hamiltonian defined in Eq. (3) accounts for systematic shifts in the Rabi oscillations from off-resonant driving through the expression $\hbar\tilde{\Omega}_m^{m'} = \lambda_j - \lambda_i$, where eigenvalues λ_j and λ_i of H correspond to the pair of dressed states coupled by the microwave field. With this model, the magnetic field strength B and the pressure shift ν_{bg} are fitted from generalized Rabi frequencies $\tilde{\Omega}_m^{m'}$, driven at 25 microwave detunings $\Delta_m^{m'}$ spaced by 800 Hz, with center frequency $\bar{\nu}_m^{m'}$ that is near-resonant with the hyperfine transitions $\nu_m^{m'}$ [Fig. 2a]. For weak coupling ($\Omega_m^{m'} \ll f_{L,\pm}$), where it's valid to approximate $\Omega_m^{m'} = |\Omega_m^{m'}|$ in H , and when the MPE shows no dependence on $\nu_{\mu w}$, all Rabi rates in H are accurately known from these measurements using the dipole moments $\mu_m^{m'}$. This work operates close to the weak atom-microwave coupling limit, but due to the lineshape of the microwave cavity modes, there is a different MPE at each hyperfine transition frequency. We account for this by

performing four separate MPE calibrations at each microwave frequency $\bar{\nu}_m^{m'}$. While the Rabi rates $|\Omega_m^{m'}|$ evaluated about $\bar{\nu}_m^{m'}$, the pressure shift ν_{bg} , and the magnetic field strength B are fitting parameters, the corresponding arguments $\text{Arg}(\Omega_m^{m'})$ and all other complex Rabi rates in Eq. (3) at each $\nu_{\mu w}$ are calculated from these MPE calibrations using Eq. (4) with the field direction (α, β) known from the coil system. Possible systematic errors arising from additional MPE $\nu_{\mu w}$ -dependence about each $\bar{\nu}_m^{m'}$ are estimated in the Supplementary Material [45].

We perform MPE calibrations by measuring generalized Rabi frequencies $\tilde{\Omega}_m^{m'}$ at each $\bar{\nu}_m^{m'}$ and at 14 different magnetic field directions by varying β and setting $\alpha = 0$. From these 14 measurements, we fit the 5 MPE parameters $(\mathcal{B}_x, \mathcal{B}_y, \mathcal{B}_z, \phi_x, \phi_y)$ for each $\bar{\nu}_m^{m'}$ using the eigenvalues of H [Fig. 2(b-d)]. During these calibrations we leave ν_{bg} as a fitting parameter and use FID measurements to estimate B . FID systematic errors are not a concern for these calibrations since $\tilde{\Omega}_m^{m'}$ depends on $\Delta_m^{m'}$ in second-order near the transition resonance.

The FID measurements differ from the Rabi and Ramsey scalar measurements by up to 5 nT over the 14 \vec{B} directions [Fig. 4c]. Heading errors qualitatively similar to Fig. 4c are predicted from simulations in the Supplementary Material [45] using experimental parameters. Despite different systematic errors from off-resonant driving, the Rabi scalar measurements across different MPEs

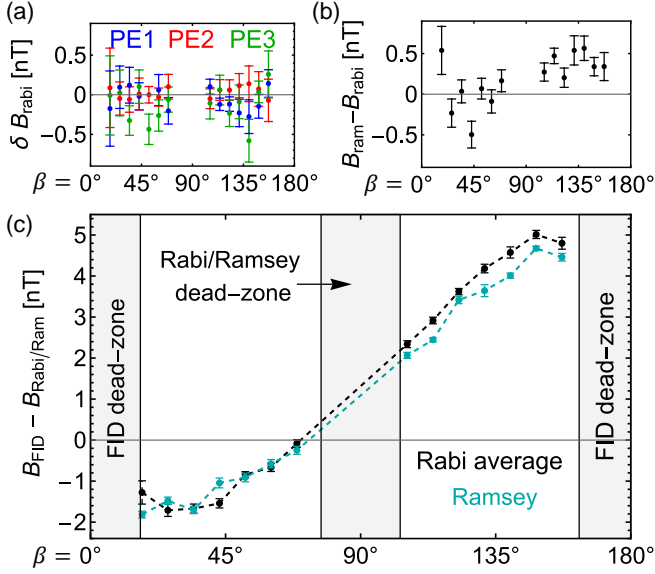


FIG. 4. Comparing FID, Rabi, and Ramsey scalar measurements over different magnetic field directions. Error bars show 68% confidence intervals. (a) Differences between Rabi scalar measurements for each MPE with respect to the average scalar across all MPEs. (b) Differences between Ramsey and Rabi scalar. (c) Differences between FID measurements with Ramsey (cyan) and Rabi (black) scalar measurements.

are consistent to within 0.5 nT [Fig. 4a]. For these Rabi measurements in Fig. 4, we only use σ^\pm transitions since we found that the π^\pm transitions are more sensitive to systematic shifts causing nT-scale discrepancies between

different MPE evaluations. This observation is consistent with theoretical simulations that account for MPE $\nu_{\mu\text{w}}$ -dependence, spin-exchange frequency shifts [43, 44], as well as lineshape distortions from atomic collisions that are detailed in the Supplementary Material [45]. From these theoretical simulations we estimate scalar errors to be contained within 0.6 nT for the Rabi and Ramsey methods. These simulations show that a large portion of errors (< 0.4 nT) arise due to frequency shifts from spin-exchange collisions. These estimates, along with drifts of the optical-pumping parameters, are consistent with the measured differences, bounded by 0.6 nT, between the Ramsey and Rabi measurements [Fig. 4b].

These results demonstrate how tailored atom-microwave interrogation through Rabi and Ramsey spectroscopy reduces OPM heading error to the sub-nT regime at geomagnetic fields and other challenging domains such as the high buffer gas pressure environments utilized in microfabricated vapor cells and regimes of weak optical pumping. Demonstration of the Rabi technique as an accurate measure via the scalar comparison establishes a solid foundation to use Rabi for accurate vector magnetometry [56].

ACKNOWLEDGMENTS

We acknowledge helpful conversations with Georg Bison, Michaela Ellmeier, Juniper Pollock, and Dawson Hewatt, and technical expertise from Yolanda Duerst, and Felix Vietmeyer. This work was supported by DARPA through ARO grant numbers W911NF-21-1-0127 and W911NF-19-1-0330, NSF QLCI Award OMA - 2016244, and the Baur-SPIE Endowed Professor at JILA.

-
- [1] I. K. Kominis, T. W. Kornack, J. C. Allred, and M. V. Romalis, *Nature*, **422**, 596-599 (2003).
 - [2] D. Budker and M. Romalis, *Nat. Phys.* **3**, 227 (2007)
 - [3] H. B. Dang, A. C. Maloof, M. V. Romalis, *Appl. Phys. Lett.* **97**, 151110 (2010).
 - [4] D. Sheng, S. Li, N. Dural, and M. V. Romalis, *Phys. Rev. Lett.*, **110**, 160802 (2013).
 - [5] G. Bison, R. Wynands, and A. Weis, *Appl. Phys. B* **76**, 325-328 (2003)
 - [6] H. Xia, A. B.-A. Baranga, D. Hoffman, M. V. Romalis, *Appl. Phys. Lett.* **97**, 151110 (2010).
 - [7] P. J. Broser, S. Knappe, D.-S. Kaja, N. Noury, O. Alem, V. Shah, and C. Braun, *IEEE Trans. Neural Syst. Rehabil. Eng.*, **26**, 2226-2230 (2018).
 - [8] J. M. Pendlebury et al., *Phys. Lett.* **13**, 327-330 (1984)
 - [9] N. J. Ayres et al., *Eur. Phys. J. C*, **81**, 512 (2021).
 - [10] M. Pospelov, S. Pustelny, M. P. Ledbetter, D. F. Jackson Kimball, W. Gawlik, and D. Budker, *Phys. Rev. Lett.*, **110**, 021803 (2013).
 - [11] S. Afach et al., *Nat. Phys.*, **17**, 1396-1401 (2021).
 - [12] M. L. Psiaki, L. Huang, and S. M. Fox, *J. Guid. Control Dyn.*, **16**, 206-214 (1993).
 - [13] A. Canciani and J. Raquet, *Navig. J. Inst. Navig.*, **63**, 111-126 (2016).
 - [14] E. Friis-Christensen and H. Lüth, G. Hulot, *EPS*, **58**, 351-358 (2006).
 - [15] C. Stolle, N. Olsen, B. Anderson, E. Doornbos, and A. Kuvshinov, *EPS*, **73**, 83 (2021).
 - [16] M. K. Dougherty et al., *Space Sci. Rev.*, **114**, 331-383 (2004).
 - [17] H. Korth, K. Strohbahn, F. Tejada, A. G. Andreou, J. Kitching, S. Knappe, S. J. Lehtonen, S. M. London, and M. Kafel, *J. Geophys. Res.: Space Phys.*, **121**, 7870-7880 (2016).
 - [18] J. S. Bennett, B. E. Vyhnaelek, H. Greenall, E. M. Bridge, F. Gotardo, S. Forstner, G. I. Harris, F. A. Miranda, and W. P. Bowen, *Sensors*, **21**, 5568 (2021).
 - [19] S. D. Billins, *IEEE Trans. Geosci. Remote Sens.*, **42**, 1241-1251 (2004).
 - [20] M. Prouty, Real-Time Hand-Held Magnetometer Array, Geometrics, Inc., (2016).
 - [21] E. B. Alexandrov, Recent progress in optically pumped magnetometers, *Phys. Scr.*, **2003**(T105), 27 (2003).
 - [22] W. Lee, V. G. Lucivero, M. V. Romalis, M. E. Limes, E. L. Foley, and T. W. Kornack, *Phys. Rev. A*, **103**, 063103 (2021).

- [23] V. Acosta, M. P. Ledbetter, S. M. Rochester, D. Budker, D. F. Jackson Kimball, D. C. Hovde, W. Gawlik, S. Pustelny, J. Zachorowski, and V. V. Yashchuk, *Phys. Rev. A*, **73**, 053404 (2006).
- [24] G. Bao, A. Wickenbrock, S. Rochester, W. Zhang, and D. Budker, *Phys. Rev. Lett.*, **120**, 033202 (2018).
- [25] G. Bao, D. Kanta, D. Antypas, S. Rochester, K. Jensen, W. Zhang, A. Wickenbrock, and D. Budker, *Phys. Rev. A*, **105**, 043109 (2022).
- [26] G. Oelsner, V. Schultze, R. IJsselsteijn, F. Wittkämper, and R. Stolz, *Phys. Rev. A*, **99**, 013420 (2019).
- [27] Y. Rosenzweig, D. Tokar, I. Shcherback, M. Givon, and R. Folman, *arXiv:2307.13982*.
- [28] S. J. Seltzer, P. J. Meares, and M. V. Romalis, *Phys. Rev. A*, **75**, 051407(R) (2007).
- [29] K. Jensen, V. M. Acosta, J. M. Higbie, M. P. Ledbetter, S. M. Rochester, and D. Budker, *Phys. Rev. A*, **79**, 023406 (2009).
- [30] Rui Zhang, Dimitra Kanta, Arne Wickenbrock, Hong Guo, and Dmitry Budker, *Phys. Rev. Lett.*, **130**, 153601 (2023).
- [31] V. M. Acosta et al., *Opt. Express*, **16**, 11423–11430 (2008).
- [32] V. V. Yashchuk, D. Budker, W. Gawlik, D. F. Kimball, Yu. P. Malakyan, and S. M. Rochester, *Phys. Rev. Lett.*, **90**, 253001 (2003).
- [33] L.M. Rushton, L. Elson, A. Meraki, and K. Jensen, *Phys. Rev. Appl.*, **19**, 064047 (2023).
- [34] A. Pollinger et al. 2018 *Meas. Sci. Technol.* **29** 095103
- [35] S.-Q. Liang, G.-Q. Yang, Y.-F. Xu, Q. Lin, Z.-H. Liu, and Z.-X. Chen, *Opt. Express*, **22**, 6837–6843 (2014).
- [36] E. Batori, C. Affolderbach, M. Pellaton, F. Gruet, M. Violetti, Y. Su, A. K. Skrivervik, and G. Mileti, *Phys. Rev. Appl.*, **18**, 054039 (2022).
- [37] C. Kiehl, D. Wagner, T.-W. Hsu, S. Knappe, C. A. Regal, and T. Thiele, *Phys. Rev. Research*, **5**, L012002 (2023).
- [38] A. Horsley, G.-X. Du, M. Pellaton, C. Affolderbach, G. Mileti, and P. Treutlein, *Phys. Rev. A*, **88**, 063407 (2013).
- [39] T. Thiele, Y. Lin, M. O. Brown, and C. A. Regal, *Phys. Rev. Lett.*, **121**, 153202 (2018).
- [40] C. Affolderbach, W. Moreno, A. E. Ivanov, T. Debogovic, M. Pellaton, A. K. Skrivervik, E. de Rijk, and G. Mileti, *Appl. Phys. Lett.*, **112**, 113502 (2018).
- [41] L. S. Cutler, C. A. Flory, R. P. Giffard, A. De Marchi, J. Appl. Phys., **69**, 2780–2792 (1991).
- [42] V. I. Yudin, A. V. Taichenachev, C. W. Oates, Z. W. Barber, N. D. Lemke, A. D. Ludlow, U. Sterr, Ch. Lisdat, and F. Riehle, *Phys. Rev. A*, **82**, 011804(R) (2010).
- [43] S. Micalizio, A. Godone, F. Levi, and J. Vanier, *Phys. Rev. A* **73**, 033414 (2006).
- [44] S. Appelt, A. B. Baranga, C. J. Erickson, M. V. Romalis, A. R. Young, and W. Happer, *Phys. Rev. A* **58**, 1412 (1998).
- [45] See Supplemental Material for additional information on the coil system calibration, data collection, Rabi frequency spectroscopy analysis, and simulations of adiabatic optical pumping, FID heading error, and systematic errors in Ramsey and Rabi frequency spectroscopy, which includes Refs. [46–55].
- [46] S. J. Seltzer, PhD, Princeton University, (2008).
- [47] Y. Horowicz, O. Katz, O. Raz, and O. Firstenberg, *Proc. Natl. Acad. Sci. U.S.A* 118 (2021)
- [48] W. Happer, Y. Y. Jau, T. Walker, *Optically Pumped Atoms* (John Wiley & Sons, 2010)
- [49] D. A. Steck, *Rubidium 87 D Line Data*, available online at <http://steck.us/alkalidata> (revision 2.2.2, 9 July 2021)
- [50] A. Pouliot, G. Carlse, H. C. Beica, T. Vacheresse, A. Kumarakrishnan, U. Shim, S. B. Cahn, A. Turlapov, and T. Sleator, *Phys. Rev. A* **103**, 023112 (2021).
- [51] E. S. Thiele Hrycyshyn and L. Krause, *Can. J. Phys.*, **48** (1970).
- [52] M. E. Wagshul and T. E. Chupp, *Phys. Rev. A* **40**, 4447 (1989).
- [53] D. K. Walter, W. M. Griffith, and W. Happer, *Phys. Rev. Lett.* **88**, 093004 (2002).
- [54] O. Katz, and O. Firstenberg, *Commun. Phys.* **2**, 58 (2019).
- [55] J. Vanier and C. Audoin, *The quantum physics of atomic frequency standards*, Vol 1 (Bristol: A. Hilger, 1989).
- [56] C. Kiehl, T. S. Menon, S. Knappe, T. Thiele, and C. A. Regal (unpublished).

Supplementary Material for “Correcting heading errors in optically pumped magnetometers through microwave interrogation”

C. Kiehl,^{1,2,*} T. S. Menon,^{1,2} S. Knappe,^{3,4} T. Thiele,⁵ and C. A. Regal^{1,2}

¹*JILA, National Institute of Standards and Technology and University of Colorado, Boulder, Colorado 80309, USA*

²*Department of Physics, University of Colorado, Boulder, Colorado 80309, USA*

³*Paul M. Rady Department of Mechanical Engineering,
University of Colorado, Boulder, Colorado 80309, USA*

⁴*FieldLine Inc., Boulder CO 80301, USA*

⁵*Zurich Instruments AG, CH-8005 Zurich, Switzerland*

CONTENTS

I. Symbol Definitions and Overview	2
II. Coil system calibration	2
III. Data collection	3
A. Ramsey measurements	3
B. Rabi measurements	3
IV. Details of Rabi frequency spectroscopy analysis	3
A. Finite impulse response (FIR) Low-pass filter	3
B. Exponentially decaying sinusoid fitting model	4
C. Calculating hyperfine transition dipole moments	4
D. Microwave polarization ellipse calibration	6
E. Fitting B from Rabi measurements	6
1. Case 1 : weak microwave field without MPE frequency dependence	6
2. Case 2 : with MPE frequency dependence	6
V. Rabi, Ramsey, and Larmor FID theoretical modeling and simulation	7
A. Optical pumping simulation of the initial atomic state ρ_i	7
1. Adiabatic optical pumping discussion	9
B. Simulated FID heading error	10
C. Theoretical model of Rabi and Ramsey measurements	10
1. Without decoherence	10
2. With decoherence and spin-exchange frequency shift	11
D. Simulate Rabi frequency spectroscopy data	12
E. Simulate Ramsey frequency spectroscopy data	14
VI. Rabi and Ramsey Systematic error discussion	14
References	16

* christopher.kiehl@colorado.edu

TABLE S1. Symbol definitions

Symbol	Definition
B	magnetic field strength
$f_{L,\pm}$	$\approx \mu_B(g_s - g_i \pm 4g_i)B/4h$ that is the mean Zeeman splitting for the $j = I \pm 1/2$ hyperfine manifolds
$\nu_{\mu w}$	microwave frequency
$\nu_m^{m'}$	microwave resonance of the $ 1, m\rangle$ - $ 2, m'\rangle$ transition
\mathcal{T}	$= \{\{1, 2\}, \{1, 1\}, \{-1, -1\}, \{-1, -2\}\}$ set of hyperfine transitions $ 1, m\rangle$ - $ 2, m'\rangle \rightarrow \{m, m'\}$
$\bar{\nu}_m^{m'}$	a selected microwave frequency near-resonant with the $ 1, m\rangle$ - $ 2, m'\rangle$ transition
ν_{bg}	buffer gas pressure shift
$\Omega_m^{m'}$	Rabi frequency coupling the $ 1, m\rangle$ - $ 2, m'\rangle$ transition
$\tilde{\Omega}_m^{m'}$	generalized Rabi frequency coupling the $ 1, m\rangle$ - $ 2, m'\rangle$ transition
$\delta\lambda_m^{m'}$	difference between eigenvalues of H corresponding to the $ 1, m\rangle$ - $ 2, m'\rangle$ transition

I. SYMBOL DEFINITIONS AND OVERVIEW

Symbol definitions used in the main text and this Supplementary Material are listed in Table S1.

II. COIL SYSTEM CALIBRATION

The coil system consists of three near-orthogonal coil pairs that generate fields along coil directions $(\vec{x}_c, \vec{y}_c, \vec{z}_c)$ given in terms of coil currents (I_x, I_y, I_z)

$$\vec{B}_{x,c} = I_x a_x (1 + \epsilon_x) \vec{x}_c \quad (S1)$$

$$\vec{B}_{y,c} = I_y a_y (1 + \epsilon_y) \vec{y}_c \quad (S2)$$

$$\vec{B}_{z,c} = I_z a_z (1 + \epsilon_z) \vec{z}_c. \quad (S3)$$

Here $(a_x, a_y, a_z) = (91.6926, 91.2159, 392.773) \mu\text{T/A}$ are pre-calibrated coil coefficients and $(\epsilon_x, \epsilon_y, \epsilon_z)$ are coil correction terms to be determined. We define this coil frame in terms of non-orthogonality angles $(\delta\theta_x, \delta\theta_y, \delta\phi_y)$ given by

$$\vec{x}_c = R_y(\pi/2 + \delta\theta_x) \hat{z} = \{\cos[\delta\theta_x], 0, -\sin[\delta\theta_x]\} \quad (S4)$$

$$\vec{y}_c = R_z(\pi/2 + \delta\phi_y) R_y(\pi/2 + \delta\theta_y) \hat{z} = \{-\cos[\delta\theta_y] \sin[\delta\phi_y], \cos[\delta\theta_y] \cos[\phi_y], -\sin[\delta\theta_y]\} \quad (S5)$$

$$\vec{z}_c = \hat{z} = \{0, 0, 1\} \quad (S6)$$

where $R_{y,z}$ are rotation matrices about the \hat{y} and \hat{z} directions.

The total field $|\vec{B}|$ generated by the coil system and a background field $\vec{B}_0 = (B_{x,o}, B_{y,o}, B_{z,o})$ is given by

$$|\vec{B}|^2 = \left(B_{x,o} + \sum_{k=x,y,z} \vec{B}_{k,c} \cdot \hat{x} \right)^2 + \left(B_{y,o} + \sum_{k=x,y,z} \vec{B}_{k,c} \cdot \hat{y} \right)^2 + \left(B_{z,o} + \sum_{k=x,y,z} \vec{B}_{k,c} \cdot \hat{z} \right)^2. \quad (S7)$$

In this framework there are 9 unknown parameters namely 3 non-orthogonality angles $(\delta\theta_x, \delta\theta_y, \delta\phi_y) = (3.68, -0.91, 3.38)$ mrad, 3 coil corrections $(\epsilon_x, \epsilon_y, \epsilon_z) = (0.82, 0.66, 2.89) \times 10^{-3}$, and three background field components $(B_{x,o}, B_{y,o}, B_{z,o}) = (-77.4, 54.4, -70.6)$ nT. We fit these 9 parameters using scalar measurements B^m extracted from FID signals by minimizing

$$C_{coil} = \sum_{j=1}^{250} (|\vec{B}|_j - B_j^m)^2 \quad (S8)$$

where j denotes a programmed current 3-tuple $(I_x, I_y, I_z)_j$ that corresponds to a random magnetic field direction $(\alpha, \beta)_j$ with norm $B_j^m \approx 50 \mu\text{T}$. The residuals of this calibration are shown in Figure S1

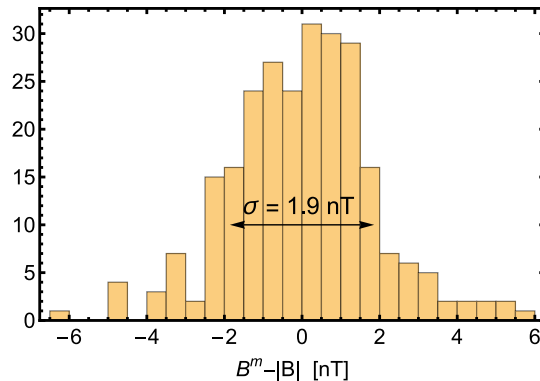


FIG. S1. Histogram of residuals between FID scalar measurements and the scalar calibration model at $50 \mu\text{T}$.

III. DATA COLLECTION

A. Ramsey measurements

Ramsey measurements at a single magnetic field direction are taken at 48 microwave detunings (12 detunings for each of the 4 hyperfine transitions). To map Ramsey fringes for each of these detunings, these measurements are divided into 124 acquisition periods corresponding to $10 \mu\text{s}$ segment increments of the Ramsey time t_R . Each acquisition period contains 3 FID measurements lasting a total of 9 ms that is followed by 48 hyper-Ramsey pulse sequences corresponding to the 48 microwave detunings that last a total of 96 ms. Thus, the total time of each acquisition period lasts 105 ms. The Ramsey times t_R for each of the 124 acquisition periods are implemented in random order. The dead time between these acquisition periods is ≈ 0.9 s. The reason for this dead time was to ensure a stable microwave cavity temperature due to the electrical heating that is turned off during the 105 ms measurement time. This means it took about 2 minutes to map all Ramsey fringes at a given magnetic field direction. For scalar averaging, we repeat each Ramsey fringe 10 times for each of the 14 magnetic field directions. Thus, all Ramsey data collection took ≈ 4.7 hours. Due to the long collection time, the Ramsey and Rabi measurements were performed on separate days.

B. Rabi measurements

All Rabi measurements required for a scalar value are taken within an acquisition period lasting 109 ms. Each acquisition period consists of 3 FID measurements lasting 9 ms that is followed by 100 Rabi measurements lasting 100 ms. These 100 Rabi measurements correspond to 25 microwave detunings for each of the 4 hyperfine transitions. For scalar averaging Rabi acquisition periods are repeated 8 times with 0.9 s deadtime between repetitions. Rabi data for all magnetic field directions took only a few minutes.

IV. DETAILS OF RABI FREQUENCY SPECTROSCOPY ANALYSIS

In this section, we provide details on the analysis of Rabi frequency spectroscopy data. First we discuss miscellaneous details of low-pass filtering of Rabi oscillation measurements, time-domain fitting, and the calculation of hyperfine transition dipole moments used to calculate Rabi rates from microwave components. Next, we discuss further details on the protocol behind microwave polarization ellipse calibration. Finally we discuss details behind the protocol to fit magnetic field strengths from Rabi measurements.

A. Finite impulse response (FIR) Low-pass filter

To remove high frequency noise and residual Larmor precession from Rabi oscillation measurements, we use a digital equiripple FIR filter of length 100, 10 kHz passband frequency, and 1 MHz stopband frequency. To implement this filter we used the Mathematica EquirippleFilterKernel function to produce the filter kernel that is convolved with

the measurement data. The impulse response of the filter is shown in Fig. S2(a,b) and its application with a Rabi oscillation measurement is shown in Fig. S2(c,d).

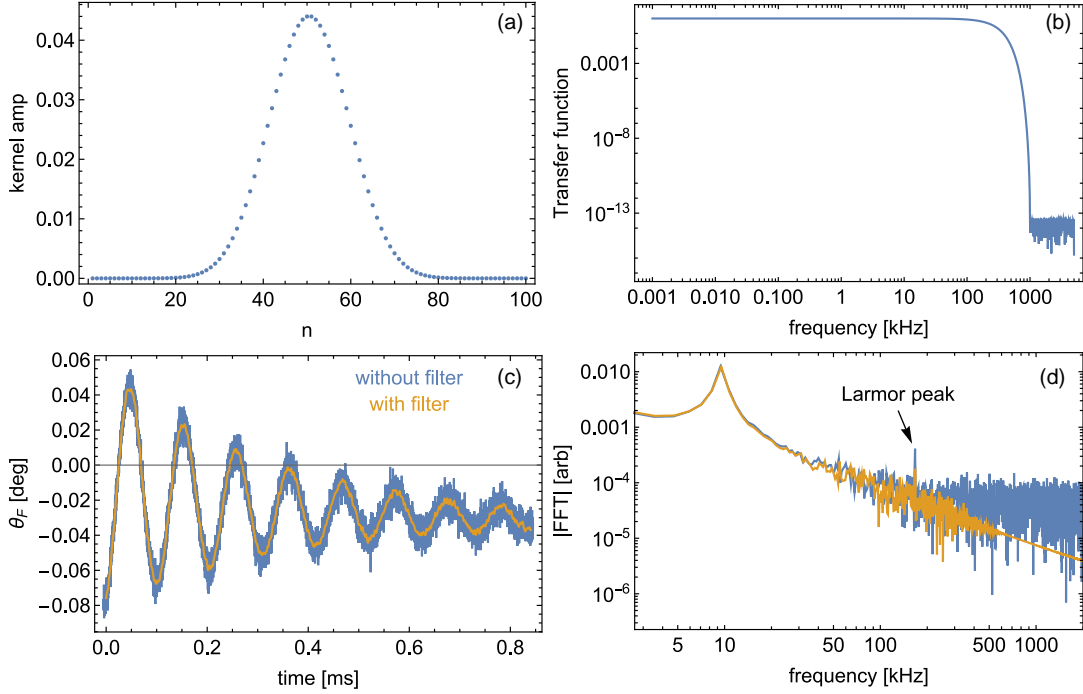


FIG. S2. (a,b) FIR filter kernel and transfer function. Rabi oscillation measurement taken at $\beta = 43^\circ$ in (c) the time domain and (d) the frequency domain.

B. Exponentially decaying sinusoid fitting model

We fit Rabi oscillations ($f \rightarrow \tilde{\Omega}$) and Ramsey fringes ($f \rightarrow \Delta_R$) using the following time-domain model

$$\theta_F(t) = a_0 + a_1 e^{-t/t_1} + a_2 e^{-t/t_2} + e^{-t/t_3} (a_3 \sin[2\pi t f] + a_4 \cos[2\pi t f]) \quad (\text{S9})$$

Here, two DC-offset decay constants t_1 and t_2 are required to account for the atomic population redistribution arising from spin-exchange collisions.

C. Calculating hyperfine transition dipole moments

The hyperfine transition dipole moments $\mu_m^{m'}$ relate the Rabi rates $\Omega_m^{m'}$ to the spherical microwave components $\mathcal{B}_{\pi,\pm}^{(\alpha,\beta)}$ through $\mu_m^{m'} = h\Omega_m^{m'}/\mathcal{B}_{\pi,\pm}^{(\alpha,\beta)}$. These transition dipole moments for the π ($m' = m$) and σ^\pm ($m' = m \pm 1$) transitions are given by

$$\mu_m^m = \mu_B \langle 2, m | \mathcal{M}(g_s S_\pi + g_i I_\pi) \mathcal{M}^\dagger | 1, m \rangle \quad (\text{S10})$$

$$\mu_m^{m\pm 1} = \frac{\mu_B \langle 2, m \pm 1 | \mathcal{M}(g_s S_\pm + g_i I_\pm) \mathcal{M}^\dagger | 1, m \rangle}{\sqrt{2}} \quad (\text{S11})$$

where $S_\pi = S_z$ and $S_\pm = S_x \pm iS_y$ are the electron-spin raising and lowering operators with analogous definitions for the nuclear-spin operators I_π and I_\pm . Table S2 tabulates these dipole moments for all $5^2S_{1/2}$ hyperfine transitions in ^{87}Rb .

Calculation of these dipole moments requires the knowledge of operator \mathcal{M} , which diagonalizes the hyperfine and Zeeman part of the Hamiltonian in Eq. (4) of the main text. While the effect of the pressure shift $\nu_{\text{bg}} \approx 88$ kHz on

TABLE S2. The magnetic transition dipole moments $\mu_m^{m'}$ for hyperfine transitions $|1, m\rangle \leftrightarrow |2, m'\rangle$. The middle column displays $\mu_m^{m'}$ in the limit of $B = 0$. The rightmost column displays the relative change in $\mu_m^{m'}$ at 50 μT given by $\delta\mu_m^{m'} = [\mu_m^{m'}(B = 50 \mu\text{T})]/[\mu_m^{m'}(B = 0)]$.

transition	$\mu_m^{m'}(B = 0)$	$\delta\mu_m^{m'} - 1$ [%]
$ 1, 1\rangle \leftrightarrow 2, 2\rangle$	$-\sqrt{\frac{3}{8}}(g_s - g_i)\mu_B$	0.42×10^{-2}
$ 1, 1\rangle \leftrightarrow 2, 1\rangle$	$\frac{\sqrt{3}}{4}(g_s - g_i)\mu_B$	-1.22×10^{-2}
$ 1, 1\rangle \leftrightarrow 2, 0\rangle$	$\frac{1}{4}(g_s - g_i)\mu_B$	-2.66×10^{-2}
$ 1, 0\rangle \leftrightarrow 2, 1\rangle$	$-\frac{\sqrt{3}}{4}(g_s - g_i)\mu_B$	1.44×10^{-2}
$ 1, 0\rangle \leftrightarrow 2, 0\rangle$	$\frac{1}{2}(g_s - g_i)\mu_B$	0.10×10^{-2}
$ 1, 0\rangle \leftrightarrow 2, -1\rangle$	$\frac{\sqrt{3}}{4}(g_s - g_i)\mu_B$	-1.63×10^{-2}
$ 1, -1\rangle \leftrightarrow 2, 0\rangle$	$-\frac{1}{4}(g_s - g_i)\mu_B$	2.47×10^{-2}
$ 1, -1\rangle \leftrightarrow 2, -1\rangle$	$\frac{\sqrt{3}}{4}(g_s - g_i)\mu_B$	0.93×10^{-2}
$ 1, -1\rangle \leftrightarrow 2, -2\rangle$	$\sqrt{\frac{3}{8}}(g_s - g_i)\mu_B$	0.61×10^{-2}

\mathcal{M} is negligible, the magnetic field-strength dependence of \mathcal{M} is also small, but not negligible. The third column of Table S2 displays the relative change of $\mu_m^{m'}$ at $B = 50 \mu\text{T}$ from $B = 0$. Table S3 shows the magnetic field-strength dependence of \mathcal{M} that is calculated by fitting polynomial terms to the \mathcal{M} -matrix elements for $B \in \{0, 1\}$ mT. The explicit functions for this magnetic field dependence are given by

$$\begin{aligned}
\mathcal{M}_{11}(B) &= 1 - 1.57774B^2 + 6.47256B^3 - 6.35276B^4 \\
\mathcal{M}_{22}(B) &= 1 - 2.10366B^2 - 0.0000379091B^3 + 24.3589B^4 \\
\mathcal{M}_{33}(B) &= 1 - 1.57774B^2 - 6.47264B^3 - 6.04991B^4 \\
\mathcal{M}_{55}(B) &= \mathcal{M}_{11}(B) \\
\mathcal{M}_{66}(B) &= \mathcal{M}_{22}(B) \\
\mathcal{M}_{77}(B) &= \mathcal{M}_{33}(B) \\
\mathcal{M}_{15}(B) &= 1.77637B - 3.64364B^2 - 0.933969B^3 + 36.1278B^4 \\
\mathcal{M}_{26}(B) &= 2.05117B + 1.16664 \times 10^{-7}B^2 - 12.9456B^3 + 0.35176B^4 \\
\mathcal{M}_{37}(B) &= 1.77637B + 3.64364B^2 - 0.933969B^3 - 36.6891B^4
\end{aligned} \tag{S12}$$

where B is in units of Tesla.

TABLE S3. The operator \mathcal{M} , that transforms the hyperfine basis $|F, m_F\rangle$ into the basis $|\overline{F}, m_F\rangle$ that diagonalizes the hyperfine and Zeeman part of the Hamiltonian defined by Eq. (4) of the main text.

	$ 1, 1\rangle$	$ 1, 0\rangle$	$ 1, -1\rangle$	$ 2, 2\rangle$	$ 2, 1\rangle$	$ 2, 0\rangle$	$ 2, -1\rangle$	$ 2, -2\rangle$
$ \overline{1}, \overline{1}\rangle$	$\mathcal{M}_{11}(B)$	0	0	0	$-\mathcal{M}_{15}(B)$	0	0	0
$ \overline{1}, \overline{0}\rangle$	0	$\mathcal{M}_{22}(B)$	0	0	0	$-\mathcal{M}_{26}(B)$	0	0
$ \overline{1}, \overline{-1}\rangle$	0	0	$\mathcal{M}_{33}(B)$	0	0	0	$-\mathcal{M}_{37}(B)$	0
$ \overline{2}, \overline{2}\rangle$	0	0	0	1	0	0	0	0
$ \overline{2}, \overline{1}\rangle$	$\mathcal{M}_{15}(B)$	0	0	0	$\mathcal{M}_{55}(B)$	0	0	0
$ \overline{2}, \overline{0}\rangle$	0	$\mathcal{M}_{26}(B)$	0	0	0	$\mathcal{M}_{66}(B)$	0	0
$ \overline{2}, \overline{-1}\rangle$	0	0	$\mathcal{M}_{37}(B)$	0	0	0	$\mathcal{M}_{77}(B)$	0
$ \overline{2}, \overline{-2}\rangle$	0	0	0	0	0	0	0	1

D. Microwave polarization ellipse calibration

The microwave polarization ellipse (MPE) calibration utilizes Rabi-frequency measurements at different magnetic field directions to calibrate the 5 MPE parameters $\mathcal{B}_x, \mathcal{B}_y, \mathcal{B}_z, \phi_x, \phi_y$ that fully define any polarization ellipse [1]. In this work, generalized Rabi frequencies are modeled through $\hbar\tilde{\Omega}_m^{m'} = \lambda_j - \lambda_i \equiv \delta\lambda_{m,m'}$, where the eigenvalues λ_j and λ_i of the atom-microwave Hamiltonian H correspond to the pair of dressed states coupled by the microwave field. Due to the fact that the magnetic field determines the atomic quantization axis, this calibration requires knowledge of the magnetic field strength B and the magnetic field direction (α, β) . For this we use the FID measurements to estimate B , and the coil system calibration to estimate (α, β) . Here we use 14 different magnetic field directions with corresponding magnetic field strengths and directions B_k and (α_k, β_k) respectively. We measure the generalized Rabi frequency driven at $\bar{\nu}_m^{m'}$ that is close to the $|1, m\rangle - |2, m'\rangle$ hyperfine resonance denoted as $\nu_m^{m'}$. We solve for free parameters $\nu_{\text{bg}}, \mathcal{B}_x, \mathcal{B}_y, \mathcal{B}_z, \phi_x, \phi_y$ with the cost function \mathcal{C}_{MPE} given by

$$\mathcal{C}_{\text{MPE}} = \sum_{k=1}^{14} w_{m,m',k} \left[\delta\lambda_{m,m'}(B_k, \nu_{\text{bg}}, \mathcal{B}_x, \mathcal{B}_y, \mathcal{B}_z, \phi_x, \phi_y, \alpha_k, \beta_k, \nu_{\mu\text{w}} = \bar{\nu}_m^{m'}) - (\tilde{\Omega}_m^{m'}) \Big|_{(\alpha_k, \beta_k)} \right]^2 \quad (\text{S13})$$

where we write $\delta\lambda_{m,m'}$ explicitly in terms of the free microwave, pressure shift, and magnetic field parameters. While we leave the buffer gas pressure shift ν_{bg} as a free parameter, these calibrations fit $\nu_{\text{bg}} \approx 88$ kHz to an accuracy within a few hundred Hz from the fact that the generalized Rabi frequencies $\tilde{\Omega}_m^{m'}$ are only measured at a single microwave frequency $\bar{\nu}_m^{m'}$ that is near resonance of the hyperfine transition. Weights $w_{m,m',k} = (1/\delta\tilde{\Omega}_m^{m'})^2 \Big|_{(\alpha_k, \beta_k)}$ are given in terms of the generalized Rabi frequency fitting error $\delta\tilde{\Omega}_m^{m'} \Big|_{(\alpha_k, \beta_k)}$.

E. Fitting B from Rabi measurements

Here, we present details behind the protocol for fitting the magnetic field strength from Rabi measurements. We first consider an ideal case of a weak microwave field and MPE parameters that do not depend on the microwave frequency. While this case is not realistic due to the lineshape of the microwave cavity modes in our experiment, it is useful to consider it because no microwave calibration is necessary. Finally, we discuss the protocol used in this work that accounts for MPE frequency dependence.

1. Case 1 : weak microwave field without MPE frequency dependence

Weak microwave driving signifies that the Rabi rates $\Omega_m^{m'}$ are small compared to the splitting between adjacent hyperfine transitions ($\Omega_m^{m'} \ll f_{L,\pm}$). In this regime, atom-microwave coupling is sufficiently modeled within the atom-microwave coupling Hamiltonian by assuming real Rabi rates, i.e., $\Omega_m^{m'} = |\Omega_m^{m'}|$. Since the microwave field parameters have no dependence on microwave frequency $\nu_{\mu\text{w}}$, the only free parameters are the magnetic field strength B , the buffer gas pressure shift ν_{bg} , and the three Rabi rates corresponding to a σ^+, σ^- , and π hyperfine transition each, such as $\Omega_+ \rightarrow \Omega_1^2$, $\Omega_\pi \rightarrow \Omega_1^1$, and $\Omega_- \rightarrow \Omega_{-1}^{-2}$. Thus, explicit knowledge of MPE parameters and the magnetic field direction (α, β) is not required. For Rabi oscillations driven on the four hyperfine transitions $\{m, m'\} \in \mathcal{T}$, these 5 free parameters could be fitted with the following cost function

$$\mathcal{C}_{B,1} = \sum_{\{m,m'\} \in \mathcal{T}} \sum_{k=-12}^{12} \left[\delta\lambda_m^{m'}(B, \nu_{\text{bg}}, \Omega_1^2, \Omega_1^1, \Omega_{-1}^{-2}, \nu_{\mu\text{w}}) - \tilde{\Omega}_m^{m'}(\nu_{\mu\text{w}}) \right]^2 \Big|_{\nu_{\mu\text{w}} = \bar{\nu}_m^{m'} + k(800 \text{ Hz})} \quad (\text{S14})$$

Here we denote the explicit ν_{μ} -dependence of the generalized Rabi frequency measurements (e.g. $\tilde{\Omega}_m^{m'} \approx \sqrt{(\Omega_m^{m'})^2 + (\nu_{\mu\text{w}} - \nu_m^{m'})^2}$).

2. Case 2 : with MPE frequency dependence

In this case, we use four MPE calibrations evaluated at the microwave frequencies $\bar{\nu}_m^{m'}$ to compensate the $\nu_{\mu\text{w}}$ -dependence of the MPE parameters. This $\nu_{\mu\text{w}}$ -dependence arises experimentally from the lineshape of the microwave cavity modes. Not taking this MPE $\nu_{\mu\text{w}}$ -dependence into account would result in errors in the modeling of frequency

shifts due to off-resonant driving. Below is the cost function $\mathcal{C}_{B,2}$ used to fit the magnetic field strength B , the buffer gas pressure shift ν_{bg} , and absolute Rabi rates $|\Omega_{+, \bar{\nu}_1^2}|, |\Omega_{\pi, \bar{\nu}_1^1}|, |\Omega_{\pi, \bar{\nu}_1^{-1}}|$, and $|\Omega_{-, \bar{\nu}_1^{-2}}|$

$$\begin{aligned} \mathcal{C}_{B,2} = & \sum_{k=-12}^{12} \bar{w}_{\sigma^+, k} \left[\delta \lambda_1^2(B, \nu_{\text{bg}}, |\Omega_{+, \bar{\nu}_1^2}| e^{i\bar{\phi}_{+, \bar{\nu}_1^2}}, \bar{\Omega}_{\pi, \bar{\nu}_1^2}, \bar{\Omega}_{-, \bar{\nu}_1^2}, \alpha, \beta, \nu_{\mu\text{w}}) - \tilde{\Omega}_1^2(\nu_{\mu\text{w}}) \right]^2 \Big|_{\nu_{\mu\text{w}} = \bar{\nu}_1^2 + k(800 \text{ Hz})} + \\ & \sum_{k=-12}^{12} \bar{w}_{\pi^+, k} \left[\delta \lambda_1^1(B, \nu_{\text{bg}}, \bar{\Omega}_{+, \bar{\nu}_1^1}, |\tilde{\Omega}_{\pi, \bar{\nu}_1^1}| e^{i\bar{\phi}_{\pi, \bar{\nu}_1^1}}, \bar{\Omega}_{-, \bar{\nu}_1^1}, \alpha, \beta, \nu_{\mu\text{w}}) - \tilde{\Omega}_1^1(\nu_{\mu\text{w}}) \right]^2 \Big|_{\nu_{\mu\text{w}} = \bar{\nu}_1^1 + k(800 \text{ Hz})} + \\ & \sum_{k=-12}^{12} \bar{w}_{\pi^-, k} \left[\delta \lambda_1^{-1}(B, \nu_{\text{bg}}, \bar{\Omega}_{+, \bar{\nu}_1^{-1}}, |\bar{\Omega}_{\pi, \bar{\nu}_1^{-1}}| e^{i\bar{\phi}_{\pi, \bar{\nu}_1^{-1}}}, \bar{\Omega}_{-, \bar{\nu}_1^{-1}}, \alpha, \beta, \nu_{\mu\text{w}}) - \tilde{\Omega}_1^{-1}(\nu_{\mu\text{w}}) \right]^2 \Big|_{\nu_{\mu\text{w}} = \bar{\nu}_1^{-1} + k(800 \text{ Hz})} + \\ & \sum_{k=-12}^{12} \bar{w}_{\sigma^-, k} \left[\delta \lambda_1^{-2}(B, \nu_{\text{bg}}, \Omega_{+, \bar{\nu}_1^{-2}}, \bar{\Omega}_{\pi, \bar{\nu}_1^{-2}}, |\bar{\Omega}_{-, \bar{\nu}_1^{-2}}| e^{i\bar{\phi}_{-, \bar{\nu}_1^{-2}}}, \alpha, \beta, \nu_{\mu\text{w}}) - \tilde{\Omega}_1^{-2}(\nu_{\mu\text{w}}) \right]^2 \Big|_{\nu_{\mu\text{w}} = \bar{\nu}_1^{-2} + k(800 \text{ Hz})} \end{aligned} \quad (\text{S15})$$

Here, we use the notation $\Omega_{\text{tr}, \bar{\nu}_m^{m'}}$ to denote a Rabi rate with $\text{tr} = \pm, \pi$ (e.g., $\Omega_+ \rightarrow \Omega_1^2$) fitted for microwave frequencies near $\bar{\nu}_m^{m'}$. We assume that the MPE parameters are constant for microwave frequencies near $\bar{\nu}_m^{m'}$. Section VI explores potential systematic errors of this assumption. The corresponding complex phases of these Rabi rates are estimated from the MPE calibrations using Eq. (5) and Eq. (6) in the main text that are denoted by $\bar{\phi}_{+, \bar{\nu}_1^2}$, $\bar{\phi}_{\pi, \bar{\nu}_1^1}$, $\bar{\phi}_{\pi, \bar{\nu}_1^{-1}}$, and $\bar{\phi}_{-, \bar{\nu}_1^{-2}}$. The remaining Rabi rates $\bar{\Omega}_{\text{tr}, \bar{\nu}_m^{m'}}$ are not fitted, but estimated from the MPE calibrated parameters. The parameters $\bar{w}_{\text{tr}, k} = 1/(\delta \tilde{\Omega}_m^{m'}(\nu_{\mu\text{w}}))^2$ are used to weight the Rabi measurements according to their fitting error. We found that only using the stretched σ_{\pm} transitions ($m' = m \pm 1$) resulted in the most accurate scalar measurements by comparing consistency in different MPE measurements, as well as consistency with Ramsey measurements. This sensitivity to the π transitions is also observed with simulated Rabi data shown in Section VI.

V. RABI, RAMSEY, AND LARMOR FID THEORETICAL MODELING AND SIMULATION

In this section we discuss the details behind simulations of the Rabi and Ramsey frequency spectroscopy protocols, as well as Larmor FID heading error. These simulations use parameters similar to those used in our apparatus with the goal of estimating the size of potential systematic errors arising from MPE frequency dependence and collisional spin-exchange frequency shifts. For these simulations, we assume that the magnetic field strength is $B = 50 \mu\text{T}$ and the buffer-gas pressure shift is $\nu_{\text{bg}} = 88 \text{ kHz}$. First, the optical-pumping model is discussed that includes optical excitation to the D1 hyperfine states. Adiabatic optical pumping is simulated to estimate the initial state ρ_i for the Rabi and Ramsey measurements at each of the 14 magnetic field directions (α, β) measured in the main text. We also discuss details behind the mechanism of adiabatic optical pumping. Next, we simulate FID heading error using experimental pumping parameters without the adiabatic power ramps. Then, using the atom-microwave Hamiltonian in Eq. (4) of the main text, we simulate the Rabi-oscillation and Ramsey-fringe signals. By using measured MPE parameters (Table S5), these simulations emulate realistic off-resonant driving.

A. Optical pumping simulation of the initial atomic state ρ_i

We utilize a mean-field approach similar to that formulated in [2, 3] to simulate the spin dynamics of the mean density matrix $\bar{\rho}$ for a single atom. The density matrix

$$\bar{\rho} = \begin{pmatrix} \bar{\rho}_{gg} & \bar{\rho}_{ge} \\ \bar{\rho}_{eg} & \bar{\rho}_{ee} \end{pmatrix} \quad (\text{S16})$$

is defined in terms of the 8 spin states in the $5^2\text{S}_{1/2}$ $F_g = 1, 2$ manifolds denoted as $\bar{\rho}_{gg}$ and the 8 spin states in the $5^2\text{P}_{1/2}$ $F_e = 1, 2$ manifolds denoted as $\bar{\rho}_{ee}$. The optical coherences are given in terms of $\bar{\rho}_{eg}$ and $\bar{\rho}_{ge}$. The master equation that governs time-evolution is given in a frame rotating with the pump optical frequency by

$$\frac{\partial \bar{\rho}}{\partial t} = -\frac{i}{\hbar} [\mathcal{H}, \bar{\rho}] + \mathcal{L}(\bar{\rho}). \quad (\text{S17})$$

TABLE S4. The different collision mechanisms, cross sections σ_i , and the calculated collision rates for a vapor cell with volume $3 \times 3 \times 2 \text{ mm}^3$, vapor temperature $T_v = 100^\circ\text{C}$, buffer gas pressure $P_{N_2} = 180 \text{ Torr}$ (24 kPa), and diffusion constant $D_0 = 0.216 \text{ cm}^2\text{s}^{-1}$ for Rb- N_2 buffer gas collisions scaled to our vapor temperature [5].

Collision type	cross-section [10^{-18} m^2]	collision rate
5P $_{1/2}$ quench (Rb- N_2)	$\sigma_q = 0.58$ [6, 7]	$\Gamma_q = n_{N_2} \sigma_q v_r = 3.2 \text{ GHz}$
5P $_{1/2}$ optical dephasing (Rb- N_2)	-	$\Gamma_o = 5.6 \text{ GHz}$ (measured)
5P $_{1/2}$ spin-destruction (Rb- N_2)	$\sigma_p = 0.64$ [3]	$\Gamma_p = n_{N_2} \sigma_p v_r = 3.5 \text{ GHz}$
5S $_{1/2}$ spin-destruction (Rb- N_2)	$\sigma_{sd} = 1.44 \times 10^{-8}$ [8]	$\Gamma_{sd} = n_{N_2} \sigma_{sd} v_r = 41 \text{ Hz}$
5S $_{1/2}$ spin-destruction (Rb-Rb)	$\sigma_{sd} = 1.77 \times 10^{-3}$ [8]	$\Gamma_{sd} = n_{Rb} \sigma_{sd} v_r = 3.6 \text{ Hz}$
5S $_{1/2}$ spin-exchange (Rb-Rb)	$\sigma_{se} = 1.9$ [9]	$\Gamma_{se} = n_{N_2} \sigma_{se} v_r = 3.89 \text{ kHz}$
5S $_{1/2}$ wall collisions	$D_0 P_0 = 0.016 \text{ m}^2\text{Torr}$ [5]	$\Gamma_D = \frac{D_0 P_0 \pi^2}{P_{N_2} (l_x^2 + l_y^2 + l_z^2)} = 0.45 \text{ kHz}$ [10]
5S $_{1/2}$ Carver (Rb- N_2)	$\Gamma_C/[N_2] = 394 \text{ amg}^{-1}\text{s}^{-1}$ [11]	$\Gamma_C = 69 \text{ Hz}$

The Hamiltonian $\mathcal{H} = H_g + H_e - \hbar \Delta I_e + V_L$ is written in terms of the ground and excited-state Hamiltonians H_g and H_e , the optical detuning $\Delta = -5.4 \text{ GHz}$ from the $|F_g = 1, 1\rangle - |F_e = 1, 1\rangle$ transition, where I_e is the excited state identity operator, and the optical coupling interaction V_L . The ground and excited-state Hamiltonians consist of the hyperfine interaction $\mathbf{A}\mathbf{I} \cdot \mathbf{S}$ and Zeeman interaction $\mu_B(g_j \mathbf{S} + g_i \mathbf{I}) \cdot \mathbf{B}$. The total energies of H_g and H_e are shifted such that at $\Delta = 0$ the energy of the ground 5S $_{1/2} |1, 1\rangle$ and the excited 5P $_{1/2} |1, 1\rangle$ states are equal. The hyperfine coupling constants and Landé g-factors are given by $A = 3.417 \text{ GHz}$ and $g_j = 2.00232$ for H_g and $A = 0.4083 \text{ GHz}$ and $g_j = 0.6659$ for H_e . In both cases $g_i = -0.00099514$. The total electron and nuclear-spin operators are denoted as \mathbf{S} and \mathbf{I} , respectively. The optical coupling $V_L = -\mathbf{E} \cdot \mathbf{D}$ is defined in terms of a complex electric field $\mathbf{E} = \{E_x, E_y e^{i\phi}, 0\}$ from the pump laser, where \mathbf{D} is the electric dipole transition operator. It is convenient to write \mathbf{E} in a spherical basis, namely $E_{\pm} = \mathbf{E} \cdot \epsilon_{\pm}$ and $E_{\pi} = \mathbf{E} \cdot \epsilon_{\pi}$ with $\epsilon_{\pm} = \{\frac{1}{\sqrt{2}}, \pm \frac{i}{\sqrt{2}}, 0\}$ and $\epsilon_{\pi} = \{0, 0, 1\}$. The matrix elements of V_L are calculated from transition dipole matrix elements

$$\langle F_g, m_{F_g} | V_L | F_e, m_{F_e} \rangle = E_k \langle F_g, m_{F_g} | e r_k | F_e, m_{F_e} \rangle / 2 \quad (\text{S18})$$

with $k = \pm, \pi$.

The relaxation operator $\mathcal{L}(\bar{\rho}) = \mathcal{L}_g(\bar{\rho}) + \mathcal{L}_e(\bar{\rho}) - \Gamma_o(\bar{\rho}_{eg} + \bar{\rho}_{ge})$ describes relaxation through radiation and collision channels in the ground and excited states, as well as optical broadening with linewidth $\Gamma_o = 5.6 \text{ GHz}$ due to Rb- N_2 collisions, respectively. Excited-state relaxation is expressed as

$$\mathcal{L}_e(\bar{\rho}) = -\Gamma_q \bar{\rho}_{ee} - \Gamma_p (\frac{3}{4} \bar{\rho}_{ee} - \mathbf{S} \bar{\rho}_{ee} \mathbf{S}) \quad (\text{S19})$$

where Γ_q is the de-excitation rate (quenching) from Rb- N_2 collisions and Γ_p is the spin-destruction (SD) rate from Rb- N_2 collisions. Relaxation in the ground manifolds is given by

$$\mathcal{L}_g(\bar{\rho}) = \frac{\Gamma_q}{\mathcal{D}^2} \mathbf{D}^\dagger \bar{\rho}_{ee} \mathbf{D} - \Gamma_{sd} (\frac{3}{4} \bar{\rho}_{gg} - \mathbf{S} \bar{\rho}_{gg} \mathbf{S}) - \Gamma_{se} (\bar{\rho}_{gg}/4 + \mathbf{S} \cdot \bar{\rho}_{gg} \mathbf{S}) (1 + 4\langle \mathbf{S} \rangle \cdot \mathbf{S}) - \Gamma_D (\rho_{gg}^e - \bar{\rho}_{gg}) \quad (\text{S20})$$

with Γ_{sd} is the spin-destruction rate due to Rb- N_2 and Rb-Rb collisions, Γ_{se} is the spin-exchange collision rate, and Γ_D is the wall collision rate. All collision rates are tabulated in Table S4. Here \mathcal{D} is the D1 transition dipole matrix element [4]

$$\mathcal{D} = \langle J = 1/2 || e r || J' = 1/2 \rangle = 2.992 e a_0. \quad (\text{S21})$$

To simulate realistic optical pumping, we use pump polarization parameters $E_y/E_x = 1.68$ and $\phi = -0.8 \text{ rad}$ measured of our pump beam in front of the vapor cell using a SK010PA-NIR polarization analyzer from Schafer and Kirchoff. The electric field norm is estimated from the laser power P given by

$$|\mathbf{E}| = \sqrt{\frac{2P}{\pi w^2 c \epsilon_0}} \quad (\text{S22})$$

assuming a Gaussian waist $w = 1 \text{ mm}$. With this model we simulate constant optical pumping for $50 \mu\text{s}$ at $P = 0.12 \text{ W}$ and then linearly ramp off the optical power over $100 \mu\text{s}$, as shown in Fig. S3(a,b). We use this model to estimate realistic initial atomic states $\rho_i = \bar{\rho}_{gg}$ at the start of Ramsey Rabi frequency spectroscopy for the 14 magnetic field directions used in this work.

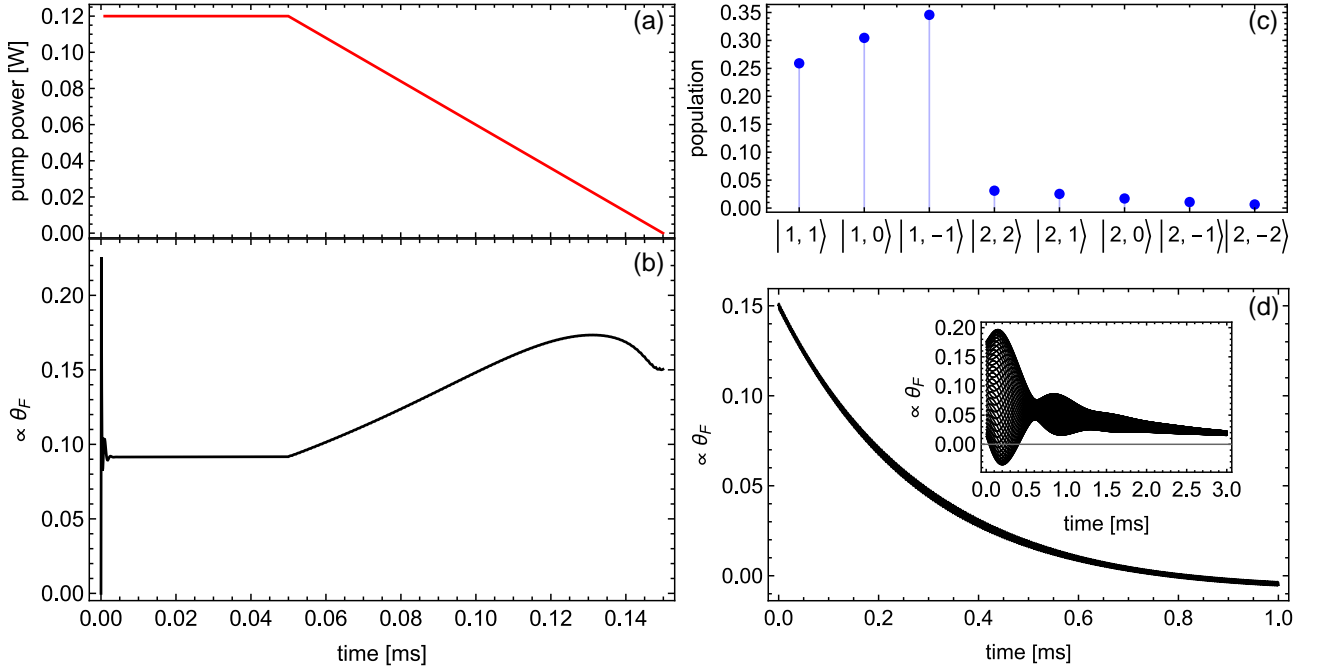


FIG. S3. Optical pump simulation for $(\alpha, \beta) = (0, 51.6^\circ)$. (a) Pump power during optical pumping simulation. (b) Simulated Faraday rotation $\theta_F \propto \langle S_z \rangle$ during optical pumping. (c) Steady-state atomic populations after adiabatic pumping. (d) spin-decay after adiabatic optical pumping shows very little Larmor precession. The inset shows resulting Larmor precession without adiabatic pump ramp shown in (a).

As a specific example of adiabatic optical pumping with the pumping model in Eq. (S17), we consider a $50 \mu\text{T}$ field with direction $(\alpha, \beta) = (0, 51.6^\circ)$. The hyperfine spin-vector \mathbf{F} after constant pumping has a steady-state direction given by $(\alpha_F, \beta_F) = (68.8^\circ, 24.6^\circ)$. Meanwhile the steady-state spin vector direction is $(\alpha_F, \beta_F) = (180^\circ - 2^\circ, 180^\circ - 52^\circ)$ rad after the linear pump ramp. Thus, after the pump ramp, the spin is nearly anti-parallel with the magnetic field, resulting in very little Larmor precession as shown in Fig. S3(c,d).

1. Adiabatic optical pumping discussion

To understand this spin-alignment with the magnetic field we consider a simpler model [7] for optical pumping

$$\frac{d\mathbf{F}}{dt} = \mathbf{F} \times \gamma \mathbf{B} + R_p(2s\hat{z} - \mathbf{F}) \quad (\text{S23})$$

where $\mathbf{F} = \{F_x, F_y, F_z\}$ is the expectation value of a generic atomic spin, γ is the gyromagnetic ratio, R_p is a pumping rate, $s \in [0, 1]$ is the degree of pump polarization, and the magnetic field $\mathbf{B} = \{B_x, 0, B_z\}$ lies in the xz -plane. In steady-state pumping $d\mathbf{F}/dt = 0$, and we can write

$$\gamma(B_x F_z \hat{y} - B_x F_y \hat{z} - B_z F_x \hat{y} + B_z F_y \hat{x}) + R_p(2s\hat{z} - \mathbf{F}) = 0. \quad (\text{S24})$$

Breaking Eq. S24 into each vector component gives

$$\begin{aligned} \hat{x}: \quad & \gamma B_z F_y - R_p F_x = 0 \\ \hat{y}: \quad & \gamma(B_x F_z - B_z F_x) - R_p F_y = 0 \\ \hat{z}: \quad & -\gamma B_x F_y + R_p(2s - F_z) = 0. \end{aligned} \quad (\text{S25})$$

The \hat{x} -equation implies $F_y = R_p F_x / \gamma B_x$. Thus, if $R_p \rightarrow 0$ adiabatically, then $F_y \rightarrow 0$. In this limit, the \hat{y} -equation predicts $B_z / B_x = F_z / F_x$. Thus, the atomic spin \mathbf{F} will align with the magnetic field \mathbf{B} assuming the pump rate R_p adiabatically turns off.

A discrepancy between the toy model in Eq. (S23) and the model in Eq. (S17) is that the toy model predicts that the spin polarization zeroes after the ramp if \mathbf{B} is perpendicular to the pump direction. Adiabatic pumping

in perpendicular magnetic fields ($\mathbf{B} \parallel \hat{x}$) with the full pumping model in Eq. S17, however, produces significant transverse electron-spin polarization $\langle S_x \rangle$, while $\langle S_{y,z} \rangle \approx 0$. We hypothesize that this effect is due to the vector light shift produced by the pumping beam, where the atomic spins adiabatically follow the effective field produced by \vec{B} and the pump light. This effect could be useful for transverse pumping applications [12].

B. Simulated FID heading error

In this section, we simulate FID heading error with parameters close to our experimental conditions. For optical pumping, we assume experimental pulse settings of 100 μs with power $P = 0.4$ W. We use the measured polarization pump parameters $E_y/E_x = 1.68$ and $\phi = -0.8$ rad discussed in Section VA. After pumping, we free-evolve the atomic state for 3 ms to generate the FID signal. We fit the resulting FID signal with the same fitting protocol described in Eq. (1) of the main text. In Figure S4 we plot the magnetic field strength error from the simulated FID signals at $B_{\text{true}} = 50$ μT for different pump detunings from $|F_g = 2, 2\rangle \rightarrow |F_e = 1, 1\rangle$ and pump relative phases from $\phi = -0.8$ rad. We explore FID heading error for different pump parameters due to the uncertainty of these parameters in our apparatus. For example, there is some uncertainty in the pump optical frequency on the order of few GHz due to the wavemeter uncertainty and drift. In addition, there is uncertainty in the pump polarization at the location of the atoms due to optical reflections off the uncoated glass walls of the vapor cell that create a small etalon. Furthermore, spatial dependence of the pump power inside the vapor cell due to absorption is not considered here. Even so, we simulate qualitatively similar heading error to our measurements in Fig. S4.

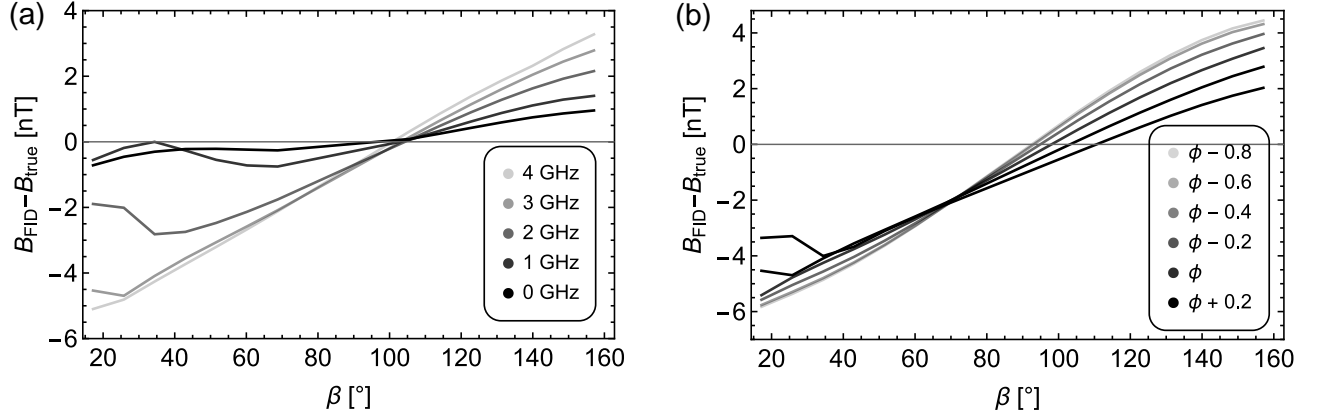


FIG. S4. Simulated FID heading error for (a) different pump detunings from $|F_g = 2, 2\rangle \rightarrow |F_e = 1, 1\rangle$ and (b) different pump relative phases from $\phi = -0.8$ rad.

C. Theoretical model of Rabi and Ramsey measurements

Next, we discuss the theoretical models describing the Rabi and Ramsey measurements. First, we describe the models without decoherence, and then discuss the full atomic state evolution with decoherence and frequency shifts from spin-exchange collisions.

1. Without decoherence

We first theoretically describe atomic state time evolution during the Ramsey and Rabi sequences without decoherence. For clarity we write the atom-microwave coupling Hamiltonian from the main text

$$H = \mathcal{M} \left[\left(A + h \frac{\nu_{\text{bg}}}{2} \right) \mathbf{S} \cdot \mathbf{I} + \mu_B (g_s S_z + g_i I_z) B \right] \mathcal{M}^\dagger - I_2 h \nu_{\mu\text{w}} + \sum_{|m-m'| \leq 1} \frac{h}{2} \left[|1, m\rangle \Omega_m^{m'} \langle 2, m'| + \text{h.c.} \right] \quad (\text{S26})$$

We denote whether the μw field is on or off ($\Omega_m^{m'} \neq 0$ or $\Omega_m^{m'} = 0$) in Eq. (S26) by H_{on} and H_{off} respectively. Let $U_t^{\text{on/off}} = e^{-iH_{\text{on/off}}t/\hbar}$ and ρ_i denote the initial atomic state immediately after optical pumping. Here ρ_i is the 8×8 density matrix of the $5S_{1/2}$ hyperfine ground states after optical pumping described in Section VA. The atomic state ρ_{rab} at time t during a Rabi oscillation is given by

$$\rho_{\text{rab}}(t) = (U_t^{\text{on}})\rho_i(U_t^{\text{on}})^\dagger. \quad (\text{S27})$$

Similarly, the atomic state ρ_{ram} at time t after the hyper-Ramsey pulse sequence is

$$\rho_{\text{ram}}(t) = (U_t^{\text{off}})(U_{t_{3\pi/2}}^{\text{on}})(U_{t_R}^{\text{off}})(U_{t_{\pi/2}}^{\text{on}})\rho_i(U_{t_{\pi/2}}^{\text{on}})^\dagger(U_{t_R}^{\text{off}})^\dagger(U_{t_{3\pi/2}}^{\text{on}})^\dagger(U_t^{\text{off}})^\dagger. \quad (\text{S28})$$

2. With decoherence and spin-exchange frequency shift

The following Liouville equation includes decoherence from spin-exchange (Γ_{se}), spin-destructive collisions (Γ_{sd}), and wall collisions (Γ_{D})

$$\frac{d\rho}{dt} = \frac{[H_{\text{on/off}} + n_{\text{Rb}}\lambda_{\text{se}}v_r\langle\tilde{\mathbf{S}}\rangle \cdot \tilde{\mathbf{S}}, \rho]}{i\hbar} + \Gamma_{\text{se}}(\tilde{\phi}(1 + 4\langle\tilde{\mathbf{S}}\rangle \cdot \tilde{\mathbf{S}}) - \rho) + \Gamma_{\text{sd}}(\tilde{\phi} - \rho) + \Gamma_{\text{D}}(\rho^e - \rho) \quad (\text{S29})$$

which is discussed in further detail in [10]. Here, $\tilde{\mathcal{O}}$ denotes operators made time-independent through the rotating-wave approximation (RWA), which is detailed in the Supplementary Material of [10]. Note that $H_{\text{on/off}}$ defined in Eq. (S26) already assumes the RWA. For these simulations we neglect Carver relaxation due to its small effect predicted for our 180 Torr buffer gas pressure [10]. Collision rates for our experimental parameters are shown in the Table S4. Here, $\phi = \rho/4 + \mathbf{S} \cdot \rho\mathbf{S}$ is known as the nuclear part of the density matrix and ρ^e is the equilibrium density matrix with all populations ρ_{ii}^e being equal.

Included in the commutator is the spin-exchange frequency shift [13, 14] $n_{\text{Rb}}\lambda_{\text{se}}v_r\langle\tilde{\mathbf{S}}\rangle \cdot \tilde{\mathbf{S}}$, which is written in terms of the Rb density n_{Rb} , the mean relative velocity v_r between Rb atoms, and the spin-exchange frequency shift cross-section λ_{se} [9]. We confirm consistency with the spin-exchange shift on the $|1, 0\rangle - |2, 0\rangle$ clock transition, predicted by [9] as a sanity check, that Eq. (S29) correctly models spin-exchange frequency shifts. For this, we evaluate

$$\frac{d\rho^{\text{wk}}}{dt} = -\frac{i}{\hbar}[H_{\text{ex}}, \rho^{\text{wk}}]. \quad (\text{S30})$$

where $H_{\text{ex}} = \hbar n_{\text{Rb}}v_r\lambda_{\text{ex}}\langle\tilde{\mathbf{S}}\rangle \cdot \tilde{\mathbf{S}}$ and ρ^{wk} is the density matrix under the weak-driving approximation that assumes fixed atomic populations and that the only non-zero off-diagonal elements are those corresponding to the clock transition

$$\rho^{\text{wk}} = \begin{bmatrix} \rho_{11} & 0 & 0 & 0 & 0 & 0 & 0 & 0 \\ 0 & \rho_{22} & 0 & 0 & 0 & \rho_{26} & 0 & 0 \\ 0 & 0 & \rho_{33} & 0 & 0 & 0 & 0 & 0 \\ 0 & 0 & 0 & \rho_{44} & 0 & 0 & 0 & 0 \\ 0 & 0 & 0 & 0 & \rho_{55} & 0 & 0 & 0 \\ 0 & \rho_{62} & 0 & 0 & 0 & \rho_{66} & 0 & 0 \\ 0 & 0 & 0 & 0 & 0 & 0 & \rho_{77} & 0 \\ 0 & 0 & 0 & 0 & 0 & 0 & 0 & \rho_{88} \end{bmatrix}. \quad (\text{S31})$$

Here, we use the index notation $|F, m_F\rangle \rightarrow i, j = 4F - m_F - 2$ for ρ_{ij} . See the Supplementary Materials of [10] for more information on the weak-driving approximation, as well as applying the RWA to the electron-spin matrices ($\mathbf{S} \rightarrow \tilde{\mathbf{S}}$). We find that evaluating Eq. (S30) gives

$$\frac{d\rho_{26}^{\text{wk}}}{dt} = -i\rho_{26}^{\text{wk}}\left[\frac{1}{4}n_{\text{Rb}}v_r\lambda_{\text{ex}}(\rho_{66} - \rho_{22})\right] \quad (\text{S32})$$

which matches the result in [9].

To calculate the Faraday rotation signal θ_F during the Rabi and Ramsey protocols, we calculate

$$\theta_F(t) \propto \text{Tr}(\rho_{\text{rab}}(t)\tilde{S}_z) \quad (\text{S33})$$

with a similar expression for $\rho_{\text{ram}}(t)$. We are careful to apply the RWA consistently to the electron-spin component S_z for calculating θ_F .

TABLE S5. Measured microwave polarization ellipse parameters for PE1, PE2, and PE3 calibrated at microwave frequencies $\bar{\nu}_m^{m'}$.

	\mathcal{B}_x [μ T]	\mathcal{B}_y [μ T]	\mathcal{B}_z [μ T]	ϕ_x [rad]	ϕ_y [rad]
$\bar{\nu}_{-1}^{-2} = 6833.7203$ MHz	1.2177	0.7973	0.01884	3.549	2.292
$\bar{\nu}_{-1}^{-1} = 6834.0701$ MHz	1.2158	0.7810	0.020	3.467	2.340
$\bar{\nu}_1^1 = 6835.472$ MHz	1.2136	0.7938	0.0207	3.445	2.373
$\bar{\nu}_1^2 = 6835.8218$ MHz	1.2100	0.8091	0.0232	3.751	2.480
$\bar{\nu}_{-1}^{-2} = 6833.7203$ MHz	0.8046	1.3086	0.0298	4.077	5.842
$\bar{\nu}_{-1}^{-1} = 6834.0701$ MHz	0.8076	1.3747	0.0221	3.764	5.538
$\bar{\nu}_1^1 = 6835.472$ MHz	0.8038	1.3021	0.0210	3.744	5.989
$\bar{\nu}_1^2 = 6835.8218$ MHz	0.7952	1.3142	0.0236	3.843	5.263
$\bar{\nu}_{-1}^{-2} = 6833.7203$ MHz	0.4125	2.0849	0.0116	3.346	2.018
$\bar{\nu}_{-1}^{-1} = 6834.0701$ MHz	0.4465	2.0543	0.0070	3.104	2.115
$\bar{\nu}_1^1 = 6835.472$ MHz	0.4402	2.0363	0.0092	3.020	2.136
$\bar{\nu}_1^2 = 6835.8218$ MHz	0.4352	2.0871	0.0033	3.229	2.025

D. Simulate Rabi frequency spectroscopy data

We simulate Rabi oscillations using Eq. (S29) at the same microwave frequencies used in the measurements, namely 25 detunings separated by 800 Hz about each $\bar{\nu}_m^{m'}$. To simulate realistic microwave interrogation we use the same microwave parameters calibrated in the experiment. These parameters for all 3 MPEs evaluated at each $\bar{\nu}_m^{m'}$ are shown in Table S5. We assume a linear drift of 0.4 % of the microwave field amplitude in these simulations to mimic possible experimental drift. This linear drift appears randomly in the analysis since the microwave frequencies are taken in random order. To simulate realistic frequency dependence of the MPE parameters, we use polynomial interpolation to estimate MPE parameters at all measured microwave frequencies about each $\bar{\nu}_m^{m'}$ shown in Fig. S5 for PE1 parameters. Such continuous frequency dependence could lead to systematic errors since Eq. (S15) only incorporates discrete PE calibrations. We examine this potential systematic error in Section VI.

Examples of simulated Rabi oscillations and corresponding generalized Rabi frequency fits at $\beta = 34^\circ$ are shown in Fig. S6(a-h). We observe small systematic errors in these fits on the order of a few Hz as shown in Fig. S6(i-l). These errors likely arise from nontrivial lineshape deviations from the exponential-decay fitting model (Eq. (S9)) due to atomic collisions, but as shown in Section VI, only cause scalar systematics at the tens of pT level (Fig. S9b).

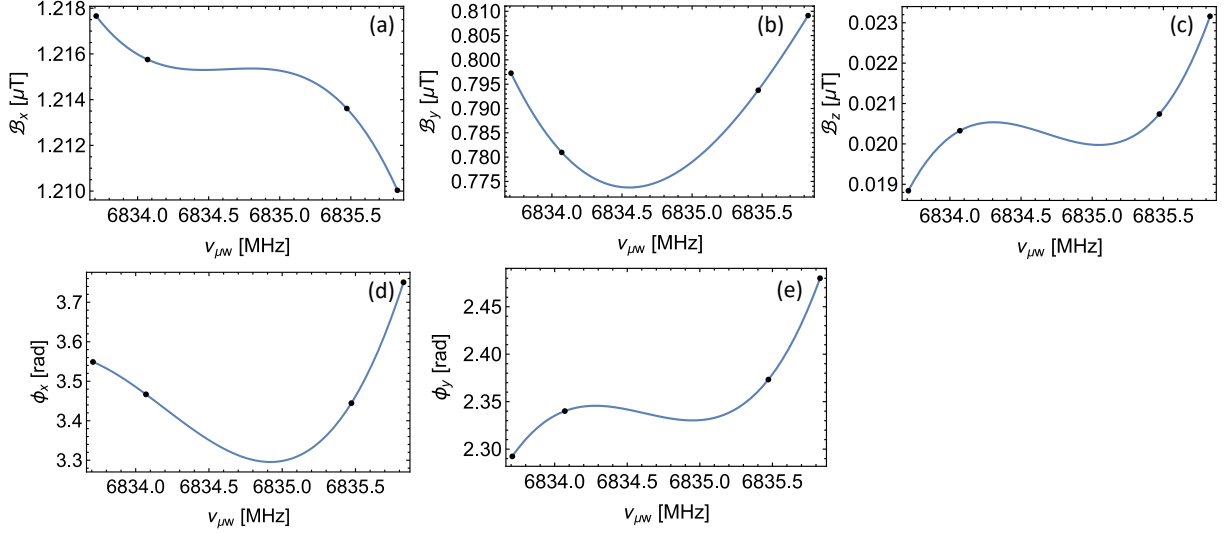


FIG. S5. Estimated frequency dependence of the 5 MPE parameters from measured calibrations (black dots) of PE1. To generate a continuous model of the frequency dependence we use polynomial interpolation of the calibrations performed at 4 different microwave frequencies. Although these polynomial interpolations are not necessarily accurate to the true frequency dependence in the experiment, they are realistic for the purposes of estimating the size of the systematic errors arising from MPE frequency dependence.

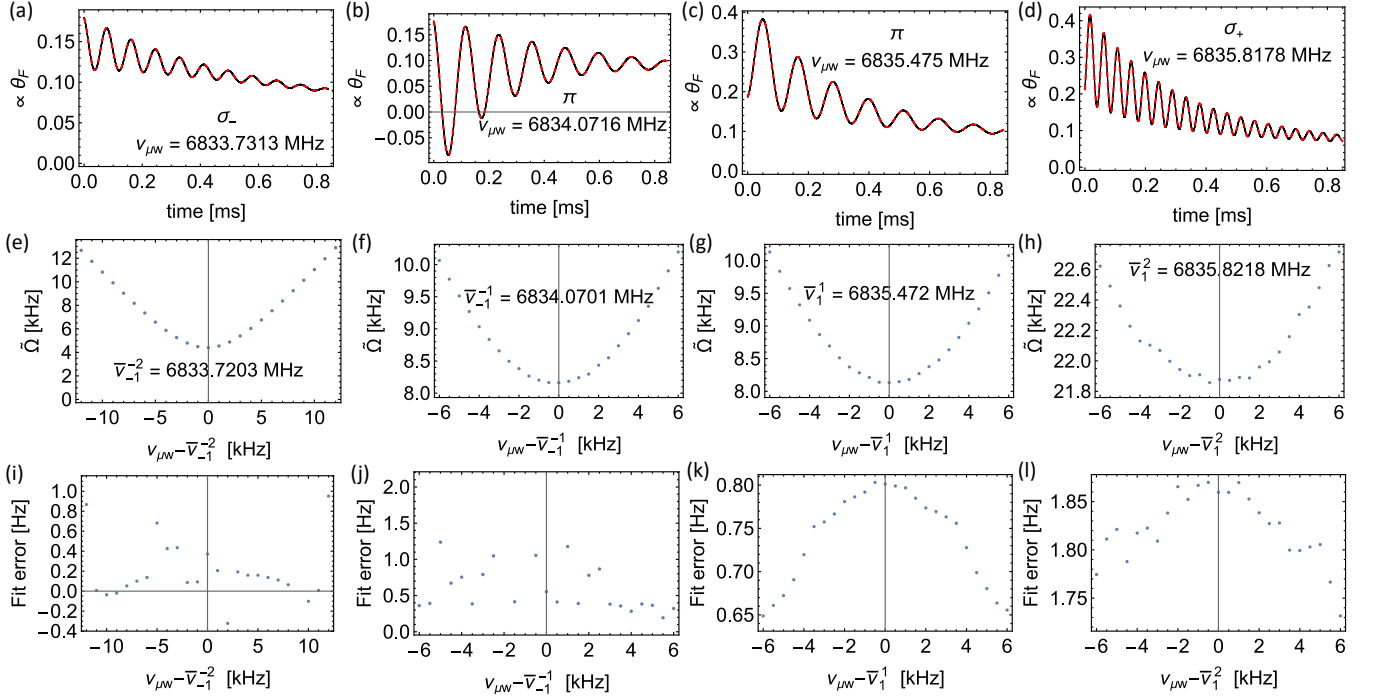


FIG. S6. Simulated Rabi oscillations and generalized Rabi frequency fits for $(\alpha, \beta) = (0, 34^\circ)$. (a-d) Simulated Rabi oscillations and fits (red dashed) for the hyperfine transitions measured in this work. (e-h) Detuning dependence of generalized Rabi frequency fits using simulated Rabi oscillations about $\bar{\nu}_m^{m'}$. The reason the detuning dependence looks funky in (h) is due to assumed microwave field amplitude drift that appears as random Rabi frequency noise. (i-l) Frequency fit errors of simulated generalized Rabi frequencies.

E. Simulate Ramsey frequency spectroscopy data

We use Eq. (S29) to simulate the $\frac{\pi}{2} - t_R - \frac{3\pi}{2}$ hyper-Ramsey sequence as shown in Fig. S7a. These simulations use the $\bar{\nu}_1^{-2}$ PE1 calibrated microwave parameters (first row of Table S5) to drive the μw pulses in the Ramsey sequence. To satisfy $t_{\pi/2} \approx 10 \mu\text{s}$ in the experiment, the power of the μw synthesizer P_{synth} at each hyperfine transition is manually chosen. To mimic this process in the Ramsey simulations, we assume that changing P_{synth} does not affect the MPE structure, but only affects the microwave amplitude $|\mathcal{B}| = \sqrt{\mathcal{B}_x^2 + \mathcal{B}_y^2 + \mathcal{B}_z^2}$. To estimate the dependence of $|\mathcal{B}|$ on P_{synth} , we measure the $\tilde{\Omega}_1^1$ generalized Rabi frequency at $\nu_{\mu\text{w}} = \bar{\nu}_1^1$ as a function of P_{synth} (Fig. S7b). Here we assume that the percent change in $\tilde{\Omega}_1^1$ gives the percent change in $|\mathcal{B}|$. Thus, from knowledge of the P_{synth} settings in the Ramsey measurements it is possible to use comparable MPE parameters in the simulations. Fig. S8 displays simulated Ramsey fringes at $\beta = 0.6$ rad with 7 kHz microwave detuning from each hyperfine transition.

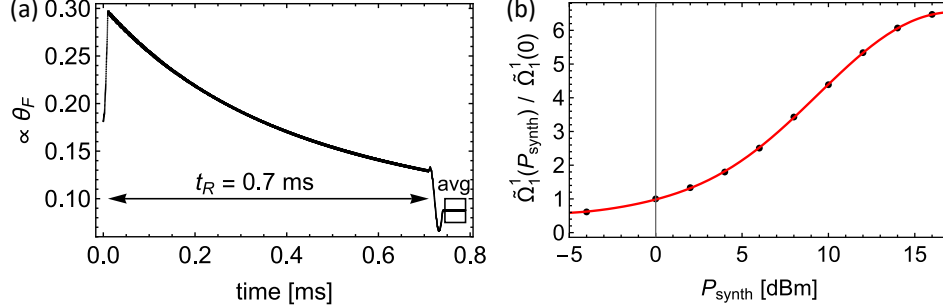


FIG. S7. (a) Simulated Ramsey pulse sequence for $t_R = 0.7$ ms at $(\alpha, \beta) = (0, 34^\circ)$. (b) estimated microwave field amplitude dependence on the power setting of the microwave synthesizer. This is estimated by measuring the change of the π generalized Rabi frequency near-resonant with $\Delta_1^1 \approx 0$ at different microwave power settings (P_{synth}).

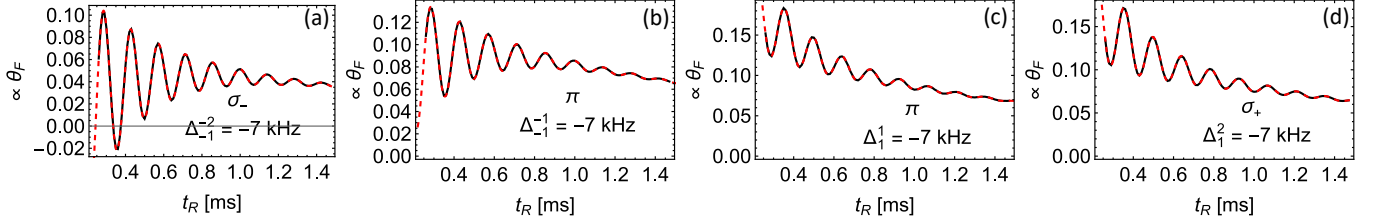


FIG. S8. Simulated Ramsey fringes with frequency fits (red dashed) for $(\alpha, \beta) = (0, 34^\circ)$.

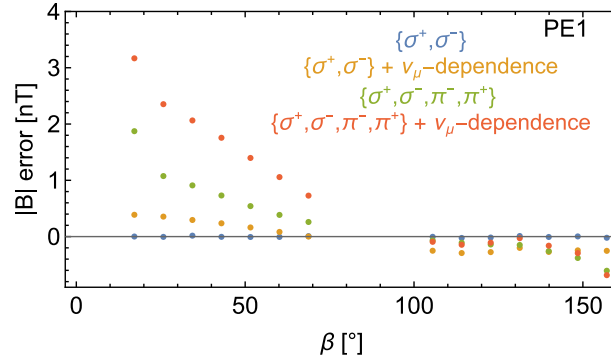
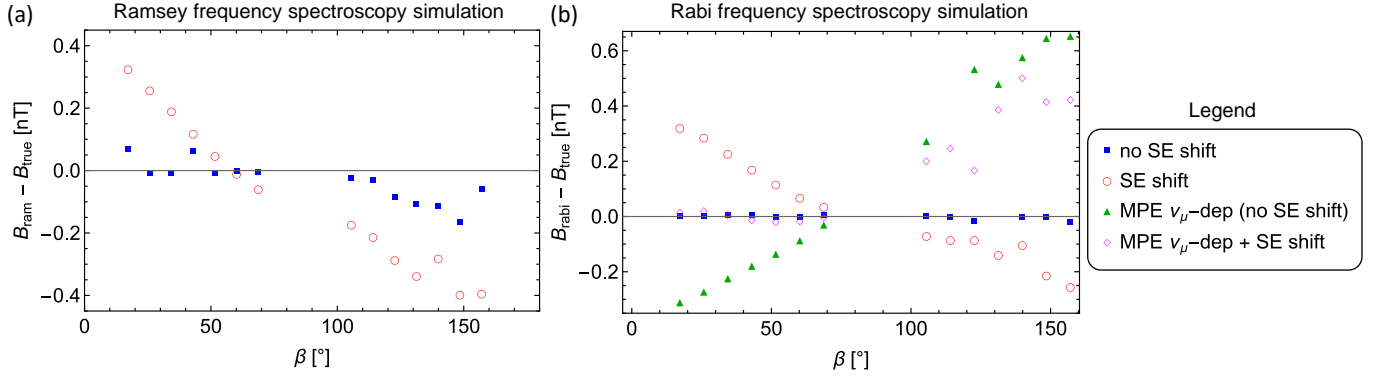
VI. RABI AND RAMSEY SYSTEMATIC ERROR DISCUSSION

We compare Rabi and Ramsey systematic errors by applying the scalar fitting protocols to simulated data discussed in Section V. Apart from systematic shifts due to off-resonant driving, Fig. S9 displays the effect of microwave-dependence and spin-exchange frequency shifts as potential sources of systematic errors. The evaluation in Fig. S9b only uses simulated σ^\pm Rabi data since including π data leads to higher systematic errors observed in simulated data shown in Fig. S10, as well as in experimental data.

Our simulations estimate that off-resonant driving leads to systematic errors on the order of 100 pT in the Ramsey frequency spectroscopy measurements as seen in the blue points of Fig. S9. Meanwhile, Rabi frequency spectroscopy has systematic errors on the order of 10 pT, which likely arise from the time-domain fitting errors attributed to collisional lineshape distortions discussed in Section VD. Including spin-exchange frequency shifts (red circles in Fig. S9) increases the Ramsey and Rabi systematic shifts to similar levels within ± 0.4 nT. For the Rabi method, the simulated microwave frequency dependence is the largest systematic error reaching 0.6 nT (green triangles in Fig. S9). This could be mitigated with improved flatness of the microwave-cavity mode. MPE frequency dependence is not expected to be a systematic for the Ramsey protocol.

From these simulations we estimate that systematic errors of the Ramsey and Rabi frequency spectroscopy are within 0.6 nT. The fact that the Rabi measurements across different MPEs and Ramsey measurements all agree to

within 0.6 nT (Fig. 4 main text) is confirmation towards this error estimate. Even so, some experimental discrepancy between Rabi and Ramsey scalar measurements could be due to experimental drift since these measurements were taken on different days.



-
- [1] T. Thiele, Y. Lin, M. O. Brown, and C. A. Regal, Phys. Rev. Lett., **121**, 153202 (2018).
 - [2] Y. Horowicz, O. Katz, O. Raz, and O. Firstenberg, Proc. Natl. Acad. Sci. U.S.A 118 (2021).
 - [3] W. Happer, Y. Y. Jau, T. Walker, Optically Pumped Atoms (John Wiley & Sons, 2010).
 - [4] D. A. Steck, Rubidium 87 D Line Data, available online at <http://steck.us/alkalidata> (revision 2.2.2, 9 July 2021).
 - [5] A. Pouliot, G. Carlse, H. C. Beica, T. Vacheresse, A. Kumarakrishnan, U. Shim, S. B. Cahn, A. Turlapov, and T. Sleator, Phys. Rev. A. **103**, 023112 (2021).
 - [6] E. S. Thiele Hryciyshyn and L. Krause, Can. J. Phys., **48** (1970).
 - [7] S. J. Seltzer, PhD, Princeton University, (2008).
 - [8] M. E. Wagshul and T. E. Chupp, Phys. Rev. A **40**, 4447 (1989).
 - [9] S. Micalizio, A. Godone, F. Levi, and J. Vanier, Phys. Rev. A **73**, 033414 (2006).
 - [10] C. Kiehl, D. Wagner, T.-W. Hsu, S. Knappe, C. A. Regal, and T. Thiele, Phys. Rev. Research, **5**, L012002 (2023).
 - [11] D. K. Walter, W. M. Griffith, and W. Happer, Phys. Rev. Lett. **88**, 093004 (2002).
 - [12] O. Katz, and O. Firstenberg, Commun. Phys. **2**, 58 (2019).
 - [13] J. Vanier and C. Audoin, The quantum physics of atomic frequency standards, Vol 1 (Bristol: A. Hilger, 1989).
 - [14] S. Appelt, A. B. Baranga, C. J. Erickson, M. V. Romalis, A. R. Young, and W. Happer, Phys. Rev. A **58**, 1412 (1998).